

1 Surface slip distributions and geometric complexity of  
2 intraplate reverse-faulting earthquakes

3

4 **Haibin Yang<sup>1</sup>, Mark Quigley<sup>1</sup>, Tamarah King<sup>1,2</sup>**

5 *Affiliation 1: School of Earth Sciences, University of Melbourne, Victoria,*

6 *Australia*

7 *Affiliation 2: COMET, Department of Earth Sciences, University of Oxford, UK*

8 [haibiny@student.unimelb.edu.au](mailto:haibiny@student.unimelb.edu.au)

9

10

11

12

13 *This manuscript has been submitted for publication in Geological Society of America*  
14 *Bulletin. Please note that, despite having undergone peer-review, the manuscript has*  
15 *yet to be formally accepted for publication. Subsequent versions of this manuscript*  
16 *may have slightly different content. If accepted, the final version of this manuscript*  
17 *will be available via the ‘Peer-reviewed Publication DOI’ link on the right-hand side*  
18 *of this webpage. Please feel free to contact any of the authors; we welcome feedback.*

19

20        **Abstract**

21        Earthquake ground surface ruptures provide insights into faulting mechanics and  
22 inform seismic hazard analyses. Surface ruptures for eleven historical (1968 to 2018)  
23 moment magnitude ( $M_w$ ) 4.7 to 6.6 reverse earthquakes in Australia are analyzed using  
24 statistical techniques and compared to magnetic, gravity, and stress trajectory datasets.  
25 Of the total combined (summative) length of all surface ruptures (~148 km), 133 km  
26 (90%) to 145 km (98%) align with geophysical structure in the host basement rocks.  
27 Surface rupture length ( $SRL$ ), maximum displacement ( $MD$ ), and probability of surface  
28 rupture at a specified  $M_w$  are high compared with equivalent  $M_w$  earthquakes globally.  
29 This is attributed to (i) steep cratonic crustal strength gradient at shallow depths  
30 promoting shallow hypocenters (~1 to 6 km) and limiting down-dip rupture widths (~1  
31 to 8.5 km), and (ii) favorably-aligned crustal anisotropies (e.g., bedrock foliations ,  
32 faults, fault intersections) that enhance lateral rupture propagation and/or surface  
33 displacements. Combined (modeled and observed)  $MDs$  are in the middle third of the  
34  $SRL$  with 68% probability, and either the  $\leq 33^{rd}$  and  $\geq 66^{th}$  percentiles of  $SRL$  with 16%  
35 probability.  $MD$  occurs proximate to or directly within zones of enhanced fault  
36 geometric complexity (as evidenced from surface ruptures) in 8 of 11 earthquakes  
37 (73%).  $MD$  can be approximated by  $3.3 \pm 1.6 (1\sigma) \times AD$  (average displacement). S-  
38 transform analysis indicates high-frequency slip maxima also coincide with fault  
39 geometric complexities, consistent with stress amplifications and enhanced slip  
40 variability due to geometric and kinematic interactions with neighboring faults. Rupture  
41 slip taper angles exhibit large variations (-90 % to + 380 % with respect to the mean

42 value) towards rupture termini and are steepest where ruptures terminate at obliquely-  
43 oriented magnetic lineaments and/or lithology changes. Incremental slip approximates  
44  $AD$  between the 10<sup>th</sup> and 90<sup>th</sup> percentiles of the  $SRL$ . The average static stress drop of  
45 the studied earthquakes is  $4.8 \pm 2.8$  MPa. A surface rupture classification scheme in  
46 cratonic stable regions is provided to describe the prevailing characteristics of intraplate  
47 earthquakes across diverse crustal structural-geophysical settings. New scaling  
48 relationships and suggestions for logic tree weights are provided to enhance  
49 probabilistic fault displacement hazard analyses for bedrock-dominated intraplate  
50 continental regions.

## 51 INTRODUCTION

52 Co-seismic ground surface ruptures on faults provide important sources of  
53 information on the seismogenic process ([Manighetti et al., 2004](#); [Wesnousky, 2008](#)).  
54 Surface rupture characteristics (e.g., maximum displacements ( $MD$ ); average  
55 displacements ( $AD$ ); surface rupture lengths ( $SRL$ )) may be combined with other  
56 seismological parameters to develop earthquake scaling relationships ([Allen et al., 2018](#);  
57 [Leonard, 2010](#); [Wells and Coppersmith, 1994](#)) for utility in probabilistic seismic hazard  
58 analyses ([Allen et al., 2018](#); [Stirling et al., 2012](#)) and probabilistic fault displacement  
59 hazard analyses (PFDHA) ([Moss and Ross, 2011](#); [Youngs et al., 2003](#)).

60 Slip distributions along surface ruptures are proposed to conform to regular shapes  
61 that relate to fracture mechanics, including elliptical shapes (linear elastic theory ([Segall  
62 and Pollard, 1980](#))), bell shapes (elastic-plastic theory ([Cowie and Scholz, 1992a, b](#))),

63 or triangular shapes (off-fault damage theory ([Manighetti et al., 2004](#)), although  
64 heterogenous stress distributions may complicate attribution of rupture shapes to a  
65 specific theory ([Bürgmann et al., 1994](#)). It is still contested whether co-seismic slip  
66 spatial distributions and associated shapes are highly variable or self-similar across  
67 different spatiotemporal scales, and what the most probable sources of variability may  
68 be ([Mai and Beroza, 2002](#); [Manighetti et al., 2009](#)). Although standard simplified  
69 shapes (e.g., ellipse or triangle) may enable generalized classification of rupture forms,  
70 empirical observations show that many ruptures include embedded hierarchical shapes  
71 in wavelength and amplitude that are described as self-similar or self-affine geometries  
72 ([King, 1983](#); [Power and Tullis, 1991](#)). Fluctuations inside the rupture plane may relate  
73 to along-strike variations in the fault roughness ([Dolan and Haravitch, 2014](#); [Gold et](#)  
74 [al., 2015](#); [Perrin et al., 2016](#); [Zinke et al., 2014](#)), the rheology of faulted materials  
75 ([Haeussler et al., 2004](#); [McGill and Rubin, 1999](#)), fault segmentation ([Brown and](#)  
76 [Scholz, 1985](#); [Klinger, 2010](#); [Manighetti et al., 2009](#); [Okubo and Aki, 1987](#)), fault  
77 junctions ([Andrews, 1989](#); [Gabrielov et al., 1996](#); [Shen et al., 2009](#)) and/or be attributed  
78 to the non-linear, anelastic responses of surficial material to sudden co-seismic strain  
79 ([Gold et al., 2015](#); [Kaneko and Fialko, 2011](#); [Zielke et al., 2015](#)).

80 The gradient with which fault slip reduces towards rupture termini (i.e., slip taper)  
81 may be linked to the interaction with periphery structures which may directly affect the  
82 earthquake arresting dynamics ([Manighetti et al., 2004](#); [Scholz and Lawler, 2004](#)). The  
83 slip taper is suggested to be a scale-invariant property of rocks ([Cowie and Scholz,](#)  
84 [1992a, b](#); [Scholz and Lawler, 2004](#)). To discern potential controlling mechanisms of

85 spatial slip gradient variation for both interior and termini, more detailed field  
86 measurements, maps, and analyses of high-resolution co-seismic slip distribution are  
87 necessary.

88 Australian stable continental regions (SCR) comprise non-extended Precambrian  
89 crust ([Leonard et al., 2014](#)) that is largely unaffected by active tectonic processes  
90 relative to plate boundaries and more rapidly deforming intraplate regions ([Johnston,  
91 1989](#)). However, Australia SCRs are not immune from seismicity. Since 1968, 11  
92 historical surface-rupturing earthquakes with moment magnitudes ( $M_w$ ) between 4.7  
93 and 6.6 have occurred in Australian SCRs ([Fig. 1A & 1B](#)) (see [King et al. \(2019\)](#) and  
94 references therein). These account for more than half of the instrumented global  
95 cratonic earthquakes ([Clark et al., 2012](#); [Crone et al., 2003](#)). Studies of the source faults  
96 suggest long (i.e.,  $>10^4$  to  $10^5$  years) preceding periods over which no surface ruptures  
97 occurred ([Clark et al., 2012](#)), which some workers have interpreted as evidence for  
98 ‘one-off’ rupture behavior on incipient or ‘newly formed’ brittle faults ([Clark et al.,  
99 2019](#); [King et al., 2018](#)). Together with the paucity of preceding, historical  $M_w > 6$   
100 events on these fault systems ([Leonard, 2008](#); [Leonard et al., 2014](#)), this suggests  
101 variations in slip rate, interseismic creep, local-to-regional stress perturbations relating  
102 to prior earthquake(s), and fault structural maturity (i.e., the roughness of the fault plane,  
103 which is physically scaled to  $D^{-0.1}$  where  $D$  is the cumulative displacement of a fault  
104 ([Brodsky et al., 2011](#))) may be of minimal significance to interpreting any slip  
105 distribution variability observed in these earthquakes. With the exception of the three  
106 surface-rupturing earthquakes on neighboring faults in the 1988 Tennant Creek

107 sequence, which have been explained by proximate Coulomb stress transfer  
108 ([Mohammadi et al., 2019](#)), 8 of the 11 Australian ruptures are thus considered to be  
109 spatially and temporally isolated, with slip distributions that are unlikely to have been  
110 strongly influenced by preceding, spatiotemporally proximate earthquakes.

111 Issues of data handling and measurement uncertainties have been recently  
112 addressed by [King et al. \(2019\)](#), who re-analyzed all Australian surface rupture  
113 displacements and established new estimates of net-slip metrics that we utilize here.  
114 Driven primarily by exploration needs of the natural resources industry, rich and diverse  
115 geophysical datasets have also been acquired and are publicly available across the  
116 continent (<https://data.gov.au/data/dataset/b0f0711d-9763-4041-9fcf-0b40bd1694a5>).  
117 [King et al. \(2019\)](#) concluded that 90% of Australian surface-rupturing earthquakes have  
118 fault orientations that align with prevailing linear anomalies in geophysical (gravity and  
119 magnetic) data and bedrock structure (foliations and/or quartz veins and/or intrusive  
120 boundaries and/or pre-existing faults), but did not consider the statistical and scaling  
121 relationships of surface rupture displacement fields in detail.

122 In this study, we propose that the shape of surface rupture displacement profiles  
123 and geometric complexity of earthquakes on incipient reverse faults emerging through  
124 SCR crust is strongly influenced by the relationships between (i) anisotropic structural  
125 and geophysical properties of the host crust that provide potential pathways for  
126 seismogenic rupture, (ii) regional stress trajectories that may be locally influenced by  
127 geologic variability, and (iii) the depth and dynamics of propagating ruptures that  
128 influence how subsurface slip is manifested at the surface. We use net displacements

129 (calculated by trigonometric analyses of vertical and lateral displacements using fault  
130 dip estimates) for 10 events from [King et al. \(2019\)](#) and convert surface offsets from  
131 the 16<sup>th</sup> September 2018  $M_w$  5.3 Lake Muir earthquake ([Clark et al., 2019](#)) to net slip  
132 assuming pure dip slip and a fault dip of 45°.

133 Rupture data is compared to the national high-resolution (grid cell size ~ 80 m)  
134 total magnetic intensity (TMI) map (<https://pid.geoscience.gov.au/dataset/ga/89596>).  
135 Since bedrock is exposed at the surface and/or is only thinly (1 to > 50 m) blanketed by  
136 aeolian and/or alluvial sediments ([King et al., 2019](#)), TMI signals directly reflect  
137 bedrock structures and lithologies in the seismogenic crust. Rock strength properties  
138 are not directly measurable by TMI, and we do not attempt to undertake a detailed TMI  
139 analysis to resolve three dimensional geometries of TMI anomalies. We focus primarily  
140 on the azimuthal relationships between surface ruptures and predominant geophysical  
141 structural-lithologic lineaments in the TMI data. The azimuthal relationship between  
142 geophysical aspects may reveal rock properties that may affect rupture propagation, e.g.,  
143 lithological boundaries or fault junctions may have lower frictional strength or modulus  
144 than intact rocks ([Gabrielov et al., 1996](#)). To locate magnetic anomalies above the  
145 source without any distortion, a variable reduction to pole is implemented in this  
146 database. Intrusive dikes of relatively lower magnetic susceptibility than host rocks  
147 have been detected through aeromagnetic mapping in the Yilgarn craton, where they  
148 are characterized by lineament anomalies ([Dentith et al., 2009](#); [Dentith et al., 2000](#)).  
149 Magnetic lineaments may represent near-vertical structures such as steep faults,  
150 plunging fold axes or intrusive dikes ([Dentith et al., 2009](#)), and these features may act

151 as stress concentrators to become the sites of subsequent faulting ([Dentith et al., 2009](#)).

152 To crudely estimate the subsurface position of rupture with respect to anomalies,  
153 we assume planar geometries with uniform dip for vertical geophysical structures.  
154 Although hypocentral depths are not resolved in high-resolution, most events have  
155 centroid moment tensor solutions and/or fault models (e.g. from InSAR) with depths of  
156 1 – 6 km indicating the earthquakes studied herein are sourced from shallow fault  
157 ruptures (e.g. [King et al. \(2019\)](#) and references therein). The shallow structures can be  
158 tracked as short wave-length responses (magnetic lineaments) in the TMI map.  
159 Additionally, national high-resolution gravity data (a grid cell size of ~ 800 m)  
160 (<https://pid.geoscience.gov.au/dataset/ga/101104>) is used to test how the gravitational  
161 body forces, which may dominate both the regional and local principal stress direction,  
162 might affect rupture complexity. Regional trajectories in maximum horizontal  
163 compressive stress ( $S_{Hmax}$ ) are taken from [Rajabi et al. \(2017\)](#).

## 164 **GEOLOGICAL SETTING**

165 All historically recorded surface-rupturing earthquakes analyzed here occurred in  
166 Australian SCRs ([Clark et al., 2012](#); [Leonard et al., 2014](#)) (Fig. 1A). The Archean  
167 Yilgarn (Fig. 1A) craton hosted the Meckering ( $M_w$  6.6, 1968), Calingiri ( $M_w$  5.0, 1970)  
168 and Cadoux ( $M_w$  6.1, 1979) events in the Southwest Seismic Zone (all earthquakes  
169 magnitudes in this paper from [Allen et al. \(2018\)](#)), which is one of the four high-  
170 seismicity zones in Australia ([Leonard, 2008](#)). The Southwest Seismic Zone (Fig. 1A)  
171 also hosted the Katanning ( $M_w$  4.7, 2007) and Lake Muir ( $M_w$  5.3, 2018) earthquakes.



172 The Proterozoic Musgrave block in Central Australia ([Fig. 1A](#)) sequentially hosted the  
173 Marryat Creek ( $M_w$  5.7, 1986), Pukatja ( $M_w$  5.2, 2012) and Petermann ( $M_w$  6.1, 2016)  
174 events. The three Tennant Creek events (Kunayungku  $M_w$  6.2, Lake Surprise West  $M_w$   
175 6.3, Lake Surprise East  $M_w$  6.5, 1988) occurred in the Paleoproterozoic Warramunga  
176 Province in the Northern Territory. Geological terrain boundaries are generally not well  
177 exposed at the surface but have been inferred from lithological, geochronological, and  
178 structure changes ([Johnston and Donnellan, 2001](#)); local structures are mapped by  
179 detailed geophysical and geological surveys ([Fig. 1C](#)). Detailed descriptions of the  
180 geological settings of each studied earthquakes are provided in [King et al. \(2019\)](#) and  
181 numerous references therein.

182

## 183 **OBSERVATIONS**

### 184 **Co-seismic slip distributions and rupture segmentation**

185 Co-seismic net-slip ([Fig. 2](#)) is mainly derived from field measurements of vertical  
186 and / or lateral discrete surface rupture displacements at surface scarps ([Clark et al.,](#)  
187 [2019](#); [King et al., 2019](#)). Net-slip for Katanning is inferred from InSAR data ([Dawson](#)  
188 [et al., 2008](#); [King et al., 2019](#)). Available displacement data for Lake Muir includes field,  
189 UAV and InSAR derived offsets ([Clark et al., 2019](#); [Dawson et al., 2008](#)). For this paper  
190 we derive net-slip from vertical offsets measured by profiles through InSAR data ([Clark](#)  
191 [et al., 2019](#)), as field/UAV data do not provide full along-rupture coverage.

192 We investigate the shape of net-slip distributions including the rupture tip taper

193 towards the ends of the faults (termini) and explore the scaling between average  
194 displacement ( $AD$ ), maximum displacement ( $MD$ ), surface rupture length ( $SRL$ ), and  
195 magnitude ( $M_w$ ) (Table S1). Since many profiles are not straight lines but rather highly  
196 curved, arcuate, and/or segmented, the  $SRL$  is the sum of different segments and / or  
197 linear approximations of the rupture trace (King et al., 2019; Table S1). Segment  
198 boundaries were previously assigned where gaps/steps exceed 1 km and/or where fault  
199 strike varies by  $>20^\circ$  in 1 km (Quigley et al., 2017). For major ruptures with parallel  
200 segment ruptures (e.g., Splinter segment in Meckering and the segment in Lake Surprise  
201 West), the net slip of each segment is projected and added to its major rupture profile.

202 Here, we describe a '*fault stepover*' as a location where the most proximate  
203 overlapping surface rupture tips are  $\geq 100$  m apart, as measured normal to the average  
204 orientation of the rupture traces (e.g., Petermann; Fig. 1). A '*fault bend*' is a location  
205 where a change in fault strike along a continuously mapped surface rupture trace is  $\geq$   
206  $20^\circ$  (e.g., Pukatja; Fig. 1). A '*fault intersection*' is a location where two faults with  
207 distinctly oriented rupture traces intersect at an angle of  $\geq 20^\circ$  (e.g., Meckering, Cadoux,  
208 Marryat Creek; Fig. 1). Some locations along a rupture trace may defined as both bends  
209 and step-overs (e.g., Calingiri, Pukatja, Fig. 2). Details of slip distributions and rupture  
210 segmentation are further described by King et al. (2019).

211 The Australian earthquake surface rupture patterns are relatively complex when  
212 compared with recent global compilations of 135  $M_w$  4.1 to 8.1 continental earthquakes  
213 (Quigley et al., 2017) (Fig. 1D). Rupture complexity is defined by the number of  
214 kinematically and structurally-distinct fault segments that ruptured in a 'single

215 earthquake', which is defined as a continuous seismic energy release with no temporal  
216 gaps in seismic moment release rate  $> 20$  seconds. An example of how this modifies  
217 previous treatment of these data is the 1988 Tennant Creek earthquake sequence (Fig.  
218 1C), where multiple mainshocks and surface ruptures were previously amalgamated  
219 into a single event (Wells and Coppersmith, 1994; Wesnousky, 2008) despite the  
220 earthquakes occurring several hours apart within a 12-hour period and producing  
221 independent scarps (Bowman, 1992). Therefore, we treat them as three separate events  
222 of  $M_w = 6.2$  (Kunayungku), 6.3 (Lake Surprise West) and 6.5 (Lake Surprise East) with  
223 their own surface rupture traces (Mohammadi et al., 2019). Three of those  $M_w > 5.7$   
224 events (Cadoux, Meckering, Marryat Creek in Fig. 1D) represent the maximum  
225 complexity for corresponding  $M_w$  in the global database (Quigley et al., 2017).

226

### 227 **Shape, symmetry and slip taper of co-seismic slip distributions**

228 To determine whether surface rupture displacement distributions can be well fit by  
229 standard shapes (Bürgmann et al., 1994; Manighetti et al., 2004; Segall and Pollard,  
230 1980), we fit various regression curves to slip data using the fit function (*fit object*) in  
231 the MATLAB curve fitting toolbox  
232 (<https://www.mathworks.com/products/curvefitting.html>). Where large gaps exist  
233 between the original observations, we linearly interpolate net-slip between the two  
234 nearest raw data. From this we set a uniform sampling distance of 0.1 km and calculate  
235 average displacement (inclusive of interpolated points). Field measurements are coded

236 with grey colors, and interpolated data are coded with red colors in [Fig. 2](#).

237 Following [Wesnousky \(2008\)](#), we fit offset data using a flat line (i.e.,  $AD$ ) and  
238 symmetric and asymmetric forms of a triangle and ellipse. For symmetric fittings, the  
239 apex (modelled  $MD$ ) is located at the rupture mid-point and is the only free variable.  
240 For asymmetric triangle forms, the modelled  $MD$  and its position are free in regression.  
241 For asymmetric ellipse forms, we follow [Wesnousky \(2008\)](#); the shape function is  
242 multiplied by a value  $(1 - m \times x)$ , where  $x$  is distance (normalized to rupture length)  
243 along the rupture, and  $m$  is the variable in regression. The parameter  $m$  and the  
244 amplitude are two free variables in the asymmetric ellipse function.

245 We first evaluate goodness of fit using the adjusted  $R^2$ , which considers the number  
246 of free variables in regression to assess the goodness of fit ([Fig. 3A](#)). Adjusted  $R^2$  is  
247 correlated with the goodness of fit;  $0.5 \leq R^2 \leq 1$  values are crudely considered to  
248 represent a good fit of a specified shape function to the empirical displacement data  
249 relative to lower  $R^2$ . Because  $R^2$  is not a good independent evaluative measure of  
250 goodness of fit for horizontal lines, we also use root mean square error (RMSE)  
251 normalized to the mean displacement ( $AD$ ) for each earthquake ([Fig. 3B](#)), to enhance  
252 our statistical comparison amongst earthquakes of different size. Normalized RMSE  
253 decreases with increasing goodness of fit ([Fig. 3B](#)).

254 Asymmetric triangle and ellipse shapes ubiquitously exhibit higher  $R^2$  and lower  
255 RMSE relative to their symmetric equivalents because they have more allowable free  
256 parameters to enhance the goodness of fit. However, some earthquakes (e.g., Katanning,  
257 Kunayungku, Meckering) exhibit high  $R^2$  and low RMSE for all shapes relative to the

258 flat-line *AD* profile ('average' in Fig. 3a, b), with small statistical preference towards  
259 asymmetric shapes. Other earthquakes are almost equally poorly fit by symmetric,  
260 asymmetric, and *AD* shapes (e.g., Petermann, Lake Surprise West, Lake Surprise East);  
261 in these instances, displacement profiles can be generalized by the *AD*. Some  
262 earthquakes are statistically poorly fit by most or all shapes (e.g., Cadoux, Pukatja) but  
263 are best represented by asymmetric triangular fits. The Marryat Creek earthquake is  
264 approximately equally well fit by asymmetric triangular and elliptical fits.

265 We further investigate the symmetry of surface rupture displacement profiles by  
266 determining the location of the apex of best-fitting asymmetric triangular and elliptical  
267 functions (i.e., the modelled *MD*) relative to the normalized surface rupture half-length  
268 (Fig. 3C). Importantly, the location and value of the observed *MD* may differ from  
269 modelled *MD* (e.g., Calingiri, Lake Muir) as the former may be strongly influenced by  
270 changes in fault geometry or interactions, while latter represents a generalized fit to the  
271 displacement profile (Fig. 2). Further, if modeled shapes are of low curvature, there  
272 may be little significance in the relative position of an apex of the best fit triangle or  
273 ellipse along the rupture profile.

274 We thus refine our definition of rupture symmetry. '*Symmetric ruptures*' contain  
275 *MD* within the middle third of the rupture trace (light blue and purple shade, Fig. 2) and  
276 have best-fitting shape symmetry  $\geq 0.33$  in Fig. 3C. Fig. 2 shows  $n = 8$  from observed  
277 *MD* (73% of total) and Fig. 3C shows  $n = 7$  (64%) ruptures with best-fitting shape  
278 symmetry  $\geq 0.33$  (Table S2). The Marryat Creek earthquake is counted in the symmetric  
279 category. The most symmetric of these (Kunayunku, Meckering, Lake Surprise East;

280 Table S2) have  $MD$  in the middle quintile of the rupture trace (light blue shade in Fig.  
281 2 and symmetry  $\geq 0.4$  in Fig. 3C). ‘Asymmetric ruptures’ have  $MD$  in the end thirds of  
282 the rupture trace (Fig. 2;  $n = 3$  observed  $MD$ ) and best-fitting symmetry values of  $<$   
283  $0.33$  ( $n = 4$ ; Fig. 3C; Table S2). The most asymmetric ruptures are the Pukatja, Calingiri,  
284 and Cadoux earthquakes (Fig. 3C). Collectively, if the two different measures of  
285 symmetry are combined, 68% of rupture displacement scenarios are ‘symmetric’, and  
286 32% are asymmetric, which equates to the probability of a  $MD$  (observed + modeled)  
287 being located in the  $\leq 33^{\text{rd}}$ , 33-66<sup>th</sup> (middle third) and  $\geq 66^{\text{th}}$  percentiles of rupture length  
288 as 16%, 68%, and 16% respectively.

289 We also calculate  $AD : MD$  ratios (Table S1) for each earthquake, for comparison  
290 with global datasets (e.g. Wells and Coppersmith (1994); Moss and Ross (2011)). These  
291 range from 0.13 (Petermann earthquake) to 0.67 (Katanning) with a mean of 0.38. The  
292 relationships between slip at a discrete location along the  $SRL$  (e.g., for utility in  
293 PFDHA) relative to  $AD$  and rupture displacement shape are explored further in the  
294 *Discussion*.

295 The rupture slip taper describes the gradient of decreasing slip towards the terminus  
296 of a fault surface rupture trace (Fig. 3D inset) (Scholz and Lawler, 2004). Asymmetric  
297 triangle fits are used to estimate discretized profile-scale slip gradients towards rupture  
298 termini. Using these functions enables good fits to be produced for some profiles but  
299 may overly smooth the data for some events. This approach minimizes the over-reliance  
300 on individual measurements which may have low signal to noise ratios and misrepresent  
301 slip tapers. To refine slip taper estimates for some specific events, we manually fit data

302 using linear regressions to local gradients at rupture termini (thick lines of blue color in  
303 [Fig. 2](#)), including two termini of the Lake Surprise East event, the right end of  
304 Katanning, and the left ends of the Petermann and Cadoux events ([Fig. 2 & 3D](#)).

305 We find an anomalously high value of net-slip 1.5 km from the south termini of the  
306 Meckering rupture. We lack confidence in the reliability of the original 1.26 m vertical  
307 offset measurement ([Gordon and Lewis, 1980](#)) because it is 0.9 – 1.0 m higher than  
308 adjacent measurements, and our inspection of SRTM elevation profiles across the  
309 projected location of the scarp (<http://pid.geoscience.gov.au/dataset/ga/72759>) reveals  
310 that no scarp of this height is visible (scarp heights of 1 – 2 m are identifiable elsewhere  
311 along the rupture). We therefore exclude this measurement from our slip taper  
312 calculation but retain it for *AD* estimations as it contributes only ~1% variance to the  
313 *AD* estimate and is thus negligible in statistical effect.

314 Rupture tip taper results are in the range of  $2.7 (\pm 1.5) \times 10^{-4}$  ([Fig. 3D](#)). Outliers  
315 with anomalously steep tapers are the asymmetric Pukatja (right = east end), Lake  
316 Surprise East (both ends) and Calingiri (left = south end) ruptures. Since these slip  
317 tapers are calculated for individual earthquakes, the estimates can be compared to  
318 ‘*isolated*’ and ‘*interacting*’ earthquake tip tapers in the dataset of [Scholz and Lawler](#)  
319 [\(2004\)](#). The average taper value for the eleven Australian earthquakes studied here ( $2.7$   
320  $(\pm 1.5) \times 10^{-4}$ ) is consistent with (albeit slightly higher than) the reported average value  
321 of  $1.8 (\pm 0.97) \times 10^{-4}$  for ‘*isolated exterior earthquake tips*’ near the end of ruptures that  
322 are unlikely to be affected by proximal fault interaction ([Scholz and Lawler, 2004](#)). Tip  
323 taper outliers from the interacting faults in our study (i.e., the Lake Surprise W and E)

324 are consistent with the [Scholz and Lawler \(2004\)](#) average taper for ‘*interacting exterior*  
325 *earthquake tips*’ of  $1.4 (\pm 1.3) \times 10^{-3}$ .

326 We acknowledge the tip tapers described here are all from reverse faults, while  
327 those in [Scholz and Lawler \(2004\)](#) are from normal-faulting or strike-slip events. The  
328 similar taper estimates suggest similar slip taper values may be observed across diverse  
329 kinematic modes of rupture and may exhibit scale independence. The prevailing  
330 characteristics of surface rupture displacement fields (shape, symmetry, slip tapers)  
331 relative to seismological attributes of the associated earthquakes and crustal structure  
332 are discussed in more detail in the *Discussion*.

### 333 **Seismological attributes: epicenter locations, source dimensions, stress drops**

334 We estimate a preferred epicenter location along each rupture profile to determine  
335 whether any relationships are evident between probable earthquake nucleation locations  
336 and slip distributions ([Fig. 2](#)). Earthquake epicenters in Australian SCRs can have large  
337 location uncertainties (i.e.,  $\geq 5 - 10$  km), particularly for early (pre-1980) and remote  
338 events due to the sparse instrumentation of the Australian National Seismograph  
339 Network (<https://www.fdsn.org/networks/detail/AU/>).

340 Each earthquake studied here has at least three reported epicenter locations. Each  
341 reported epicenter is first projected to the nearest surface rupture location; this may be  
342 along the fault trace or a fault tip. Where epicentral locations reside at distances  $> 15$   
343 km from the rupture plane (e.g., the mis-location of initial epicenters for the Marryat  
344 Creek earthquake are  $> 30$  km from the rupture plane), these events are excluded from



345 the analysis. Revised locations for epicentral locations are used; for example ([Denham,](#)  
346 [1988](#); [McCue et al., 1987](#)) favored an epicentral location for the Marryat earthquake on  
347 the east-west oriented (W) branch ([Fig. 2](#)). We count the number of epicenters that  
348 project to each third of the rupture length and consider the rupture third with the most  
349 projected epicenters (or best constrained epicenter locations; e.g., we prefer the  
350 epicenter locations and associated uncertainties for the Tennant Creek earthquakes  
351 using [Choy and Bowman \(1990\)](#)) as the favored host third of the epicenter (horizontal  
352 double-arrowed lines in [Fig. 2](#)). If the preferred epicenter location is proximal to a  
353 boundary between adjacent rupture thirds, we include both thirds as possible hosts for  
354 the epicenter. [King et al. \(2019\)](#) present a detailed discussion of the epicenters  
355 associated with each earthquake.

356 The epicenter positions that we display in [Fig. 2](#) are the preferred host third(s) based  
357 on all reported epicenter data for each earthquake. A ‘*unilateral*’ rupture (e.g.,  
358 Katanning, Lake Surprise West, Kunayunku, Cadoux; [Table S2](#)) is defined as containing  
359 the projected earthquake epicenter in either of the end thirds of the rupture trace, a  
360 ‘*bilateral*’ rupture (e.g., Calingiri, Lake Surprise East, Petermann, Meckering; [Table S2](#))  
361 contains a projected epicenter in the middle third of the rupture. Where the projected  
362 location of the epicenter on to the rupture trace is insufficiently precise to enable  
363 designation into a specific third of the rupture (Pukatja, Marryat Creek, Lake Muir;  
364 [Table S2](#)), we do not consider it in the analysis of rupture directivity. We do not examine  
365 the vertical component of rupture propagation. Of the 8 ruptures analyzed, 50% exhibit  
366 unilateral and 50% exhibit bilateral rupture directivity, and no relationship between

367 rupture shape and epicenter location is evidenced.

368 Hypocenters for all events are subject to large locational uncertainties ( $> 5$  km) due  
369 to large distances between the instrumental networks (particularly pre-1980) and  
370 earthquake locations ([Leonard, 2008](#)). However, revised hypocenter estimates are  
371 available for most events (excluding Katanning, Pukatja and Petermann) ([Table S4](#)).  
372 Additionally, CMT depth results (location of predominant moment release) and  
373 modelled faults (e.g. InSAR inversion) are available for some faults ([Table S4](#)). These  
374 hypocentral, centroid and fault-depth estimates have a combined mean depth of  $3.6 \pm$   
375  $1.9$  km, while revised hypocenters have mean depths of  $4.4 \pm 2.1$  km. These estimates  
376 are significantly shallower than reverse-faulting earthquakes in the non-cratonic areas  
377 outside Australia with a mean of  $14 \pm 5$  km ([Wells and Coppersmith, 1994](#);  
378 [Wesnousky, 2008](#)). We do not consider the contribution of additional (epistemic)  
379 uncertainties for this data but note that shallow hypocenters are further required in the  
380 Australian examples to balance seismic moments against rupture area constraints.

381 We estimate down-dip rupture widths ( $W$ ) by averaging the results of four width  
382 estimates ([Table S3](#)) based on (a) hypocenter/CMT/fault depths with dip of  $45^\circ$  (b) same  
383 depth as (a) with preferred dips from [King et al. \(2019\)](#) (c) revised hypocenters (excl.  
384 Katanning, Pukatja and Petermann; see [Table S4](#)) with dip of  $45^\circ$  (d) same depth as (c)  
385 with preferred dips from [King et al. \(2019\)](#) (all results in [Table S5](#)).

386  $SRL:W$  ratios are estimated from our preferred widths and shown in [Fig. 2](#) ( $SRL$  is  
387 abbreviated to  $L$  in [Fig. 2](#)). Width ( $W$ ) ranges from 1.2 km (Katanning) to 11.6 km (Lake  
388 Surprise East).  $SRL:W$  ratios range from 0.2 (Pukatja) to 5.5 (Peterman), with an

389 average  $SRL:W$  of 2.4. These are generally consistent with the range of  $SRL : W$  ratios  
390 in global compilations of dip slip earthquakes over the same  $M_w$  range (0.7 to 4; average  
391 1.5) ([Weng and Yang, 2017](#)).  $SRL:W$  ratios exceed 2.0 in 55% of events. The three  
392 earthquakes with longest  $SRL$  yield the three largest  $SRL:W$  ratios. The variability in  
393  $SRL:W$  ratios in this small dataset can be considered high when compared with global  
394 data.

395 Stress drops have been reported for several of the earthquakes studied here ([Fig. 2](#)  
396 [caption](#)). It is critical to first acknowledge that stress drops can be estimated via a variety  
397 of methods, including (i) static shear stress drop ( $\Delta\sigma^s$ ) from established equations (e.g.,  
398 [Starr \(1928\)](#)) that include average fault displacements (e.g., ~9 MPa for Meckering and  
399 Caligiri; [Denham et al. \(1980\)](#)), and (ii) dynamic stress drops estimated from source  
400 time functions (e.g., ca. 5.8 to 13 MPa for the Tennant Creek earthquakes; [Choy and](#)  
401 [Bowman \(1990\)](#)). Secondly, stress drop estimates are highly sensitive to estimates of  
402 rupture size and slip, and variations in fault rock shear strength, and are therefore  
403 accompanied by large (and typically uncharacterized) uncertainties both in absolute  
404 value and in spatial distribution ([Dawson et al., 2008](#); [Denham et al., 1987](#)). Third,  
405 stress drops have not been established for all earthquakes studied here and thus there is  
406 epistemic uncertainty in how to compare one earthquake with another in this aspect.  
407 The highest reported  $\Delta\sigma^s$  estimates are 14-27 MPa for the Katanning earthquake  
408 ([Dawson et al., 2008](#)), and the lowest (ca. 2 MPa) are for the Petermann and Cadoux  
409 earthquakes ([Attanayake et al., 2020](#); [Denham et al., 1987](#)) ([Table S1](#)). Given these  
410 uncertainties and variance, ensemble modeling of stress drops using a variety of source

411 fault characteristics and other input parameters is warranted.

412 We model  $\Delta\sigma^s$  for all earthquakes by averaging the results from four stress drop  
413 estimates which include: the method from [Madariaga \(1977\)](#) using seismic moment  $M_0$   
414 (estimated from  $M_W$ ),  $W$ , and fault area (assuming an elliptical fault); the method of  
415 ([Griffith et al., 2009](#)) based on [Madariaga \(1977\)](#) using  $AD$ ,  $W$ ,  $L$ , with 20 GPa and 50  
416 GPa shear modulus ( $\mu$ ) ([Zhao and Muller, 2003](#)); and published stress drops ([Table S1](#)).  
417 The full results of these estimates are detailed in [Table S6](#) and [Figures S1](#) and [S2](#).

418 Our  $\Delta\sigma^s$  range from  $1.5 \pm 0.9$  MPa (Marryat Creek) to  $9.5 \pm 5.9$  MPa (Lake Surprise  
419 West) with a mean of  $4.8 \pm 2.8$  ( $1 \sigma$ ) MPa. These vary from previously reported  $\Delta\sigma^s$   
420 ([Table S1](#)) by 21 % (Cadoux) to 56% (Katanning) (note that our calculations  
421 incorporate these previously published data).

422 Cratonic *in situ* stresses have relevance to discussions on the seismological  
423 characteristics of these earthquakes. Proxy measurements of stresses at 0 to 1.5 km  
424 depth (extrapolation to greater depths) imply large increases in maximum horizontal  
425 and deviatoric stresses from the surface (ca. 5 to 20 MPa), to ca. 1.5 km depth (ca. 100  
426 MPa; [Bamford \(1976\)](#)) and to depths of ca. 5 km (ca. >200 MPa; [Denham et al. \(1980\)](#)).  
427 The possibility that stress drops exhibit an aspect of depth-dependence is considered in  
428 this context ([Huang et al., 2017](#)).

429

### 430 **S-transform analysis of the slip residuals**

431 Earthquake slip distributions commonly exhibit aspects of hierarchical self-

432 similarity or self-affinity ([Frankel, 1991](#); [King, 1983](#); [Mai and Beroza, 2002](#)) that  
433 manifest as low amplitude and short wavelength features (i.e., low level shapes)  
434 embedded into the high amplitude and long wavelength first-order shape of the total  
435 displacement field (i.e., the basic shape).

436 To investigate the spectral characteristics and distributions of low level shapes, we  
437 first subtract the basic shape component from the discrete observations and apply S-  
438 transform analyses on the residuals ([Stockwell et al., 1996](#)). The basic shape (triangle  
439 or ellipse) is selected by the shape fitting with higher  $R^2$  ([Fig. 2](#)). The S-transform is  
440 based on the idea of the continuous wavelet transform and has a moving and scalable  
441 localizing Gaussian window. The advantage of the S-transform is that it can deal with  
442 non-stationary signals (like the slip distributions in this study), and provide a clear  
443 space-frequency representation of the slip distribution, which is not available for the  
444 classical Fourier spectrum method.

445 The S-transform given by [Stockwell et al. \(1996\)](#) is expressed as  $S(l, k) =$   
446  $\int_{-\infty}^{\infty} h(x) \frac{|k|}{\sqrt{2\pi}} e^{-(l-x)^2 k^2} e^{-i2\pi kx} dx$ , where  $S$  is the S-transform of the space function  
447  $h(x)$ , which is the residual spatial distribution;  $k$  is the spatial frequency and  $l$  is the  
448 parameter which determines the position of the Gaussian window. The window size is  
449 inversely scaled with  $k$ . The S-transform characterizes the local spectrum, and  
450 averaging the local spectra over the whole space gives the Fourier spectrum as  
451  $\int_{-\infty}^{\infty} S(l, k) dl = H(k)$ , where  $H(k)$  is the Fourier transform of  $h(x)$ . In this study,  
452  $h(x)$  of each event is normalized by the corresponding maximum residual. In the  
453 following, we first demonstrate the frequency-space distribution,  $S(l, k)$ , of the

454 residual signals, and then check its averaging representations,  $H(k)$ . A potential source  
455 of sampling bias is that some fault segments have fewer measurements relative to others,  
456 and that the slip shapes derived for the faults with sparse measurement data may be  
457 oversimplified.

458 [Fig. 4](#) shows the results of the S-transform analysis. The spatial frequency  
459 parameter  $k$  is a discretized value of  $SRL$  / the wavelength of the specified increment.  
460 For example, a value of  $k = 50$  is equal to a wavelength of 280 m for the Marryat Creek  
461 earthquake ( $SRL = 14$  km) and 780 m for the Meckering earthquake ( $SRL = 39$  km). A  
462 value of  $k = 0$  represents a rupture shape wavelength  $>1.5 SRL$  with an infinite upper  
463 limit representing a horizontal line (i.e., residuals that are collectively fit by a shape  
464 with a wavelength longer than  $SRL$ ). A value of  $k = 1$  is equivalent to fitting the  
465 displacement profile with one shape (wavelength =  $SRL$ ). As the uniform resampling  
466 interval is 100 m, the highest spatial frequency that can be recovered is 200 m. The  $z$   
467 axis is a unitless measure of the relative apportionment of energy (i.e., probability  
468 distributions) for different residual wavelengths (i.e., spatial frequencies) plotted as  
469 discrete (100m) increments along the  $SRL$ . Since the range of computable values for  $k$   
470 is conditional upon  $SRL$  and the minimum wavelength of the sampling interval, larger  
471 values of  $k$  can be estimated for longer ruptures (e.g., Meckering, Petermann) relative  
472 to short ones (e.g., Pukatja, Calingiri).

473 [Fig. 5](#) shows the averaged S-transform results  $H(k)$  over the whole rupture length  
474 ([Table S2](#)). The Pukatja earthquake exhibits minimal statistical preference amongst  $k$   
475 =1 to 4. This is consistent with (i) the highly sinuous and structurally complex surface

476 rupture morphology that could promote slip variability (manifested as embedded  
477 shorter wavelength shapes in the general profile), and (ii) the high density of surface  
478 displacement measurements, that could enhance recognition of any displacement  
479 variability ([Clark et al., 2014](#)). Enhanced high frequency energy at  $4 \leq k \leq 8$  in the  
480 eastern third of the rupture is associated with the location of peak displacement and  
481 variability at a step-over ([Fig. 1, 4](#)).

482 The Katanning earthquake exhibits clear statistical preference for  $k=1$  with small  
483 signals associated with  $k=0$  (suggestive of adherence to a broader form) and  $k=2$  and  
484 3 towards rupture termini ([Fig. 4](#)), where small fault orientation changes are possible  
485 based on InSAR data ([Fig. 1](#)) ([Dawson et al., 2008](#)) and where enhanced variability  
486 would be expected as deformation is diffused from the primary fault. This earthquake  
487 exhibits the simplest S-transform spectra and is consistent with a shallow focus, circle-  
488 shaped, structurally simple rupture ([Dawson et al., 2008](#)) although these data also  
489 reflect our utility of the INSAR-derived rupture model, given the lack of discrete field-  
490 observed surface displacements.

491 The Calingiri earthquake exhibits a statistical preference for  $k=3$  (and  $k=2$ ) above  
492  $k=1$ , consistent with the segmented rupture trace ([Fig. 1](#)) and deformation undulations  
493 at wavelengths of  $\sim 1.3$  to 2 km ([Fig. 2, 5B](#)). The zone of enhanced high frequency  
494 energy ( $8 \leq k \leq 15$  corresponding to wavelengths of 500 to 260 m; [Fig. 4, 5B](#)) is  
495 concentrated in the southern half of the rupture and is coincident with maximum  
496 displacement at a fault stepover ([Fig. 2, 4](#)).

497 The Lake Muir earthquake exhibits statistical preference for  $k=2$  (and  $k=3$ )

498 corresponding to wavelengths of 2.4 (and 3.6 km). The preference of a segmented  
499 rupture is consistent with distinctive trends in the rupture trace with  $\sim 20$  to  $45^\circ$  variance  
500 ([Clark et al., 2019](#)). Embedded shorter wavelength triangular shapes ([Fig. 2](#)) are  
501 identified at  $6 \leq k \leq 9$  (1.2 to 0.8 km wavelength) ([Fig. 4, 5A, 5B](#)) and these include  
502 additional hierarchies of embedded energy undulations at higher  $k$  ([Fig. 4](#)). High  
503 frequency energy signals coincide with peak displacement at a small fault step-over,  
504 and change in average rupture trace orientation (fault bend), in the eastern half of the  
505 rupture ([Clark et al., 2019](#)) ([Fig. 1, 2](#)).

506 The source ruptures of the 1988 Tennant Creek share similar attributes: *(i)* a clear  
507 statistical preference for low  $k$  ( $k = 1$  for Lake Surprise W and E;  $k = 2$  for Kunayungku),  
508 with progressively decreasing contributions with increasing  $k$  (particularly distinct  
509 when compared to the similarly-sized Marryat Creek and Petermann earthquakes; [Fig.](#)  
510 [4, 5A, 5B](#)), *(ii)* localized pulses of energy at high  $k$  in the central portions of rupture  
511 traces (all), coincident with peak displacements that may be associated with fault bends  
512 +/- intersections (Lake Surprise E) ([Fig. 1, 4](#)), and *(iii)* minimal energy contributions  
513 from wavelengths  $< 3$  km ([Fig. 5B](#)). In comparison, the Marryat Creek and Petermann  
514 earthquakes are characterized by *(i)* large mean energy contributions at  $k \geq 5$  in [Fig. 5A](#)  
515 (wavelength  $\sim 2$ -3 km) that are similar to the mean relative probabilities at  $k = 1$  or 2  
516 ([Fig. 5A](#)), and *(ii)* localized high  $k$  ( $> 10$ ) peaks ( $\sim 1$  km wavelengths; [Fig. 4](#)) coincident  
517 with maximum displacement domains at fault intersections (Marryat Creek) and step-  
518 overs (Petermann) ([Fig. 1, 2](#)). In addition to the distinctions, it is notable that the Lake  
519 Surprise E and W, and Petermann earthquakes exhibit less definitive shape profiles that



520 are as almost as well represented by average displacements (flat lines) as triangular or  
521 elliptical fits, whereas Kunayungku and Marryat Creek adhere more closely to  
522 asymmetric triangles.

523 The Cadoux earthquake is statistically best-defined by a single ( $k = 1$ ) asymmetric  
524 triangle displacement profile (Fig. 2, 4, 5) despite a highly complex and segmented ( $n =$   
525 6 faults; [King et al. \(2019\)](#)) rupture trace (Fig. 1), suggesting strong transfer of vertical  
526 displacement across complex fracture networks. Both the northern and southern thirds  
527 of the rupture include local slip maxima at high-angle fault intersections (Fig. 1, 2) and  
528 high  $k$  spikes associated with embedded high frequency triangular shapes (Fig. 2).  
529 Distinct from Lake Surprise W and Kunayungku, there is a persistent mean probability  
530 signal at  $2 \geq k \geq 10$  (Fig. 5); the upper range ( $k = 5$  to 10) of which corresponds with  
531 wavelengths of 4.6 to 2.3 km.

532 For the Meckering earthquake we analyze the full published dataset, without  
533 removing the anomalously high net-slip value previous discussed in the southern part  
534 of the rupture. The Meckering earthquake exhibits consistent relative probabilities for  
535  $k = 1$  and  $k = 2$ , both of which are statistically preference in the  $0 \geq k \geq 10$  range (Fig.  
536 5). A high  $k$  spike is observed at the southernmost end of the rupture (Fig. 4). The  
537 persistent signal at  $4 \geq k \geq 10$  (Fig. 5A, 5B) corresponds to contributions from  $\sim 9.8$  to  
538 3.9 km wavelengths; these are evident as hierarchical, self-similar triangle-shaped  
539 features embedded within the overall triangular-shaped slip shape (Fig. 2). The  
540 Meckering earthquake could have comprised as many as 4 to 8 planar faults (Fig. 1D);  
541 consistent with elevated signals at  $k \geq 4$ . No evidence for fault trace orientation changes

542 or fault intersections on displacements is found; the displacement profile is statistically  
543 well fit by the triangular shape function (Fig. 3).

#### 544 ***MD, SRL, and fault geometry***

545 We plot *MD* and *SRL* against  $M_w$  (Fig. 6) and compare against global thrust fault  
546 regressions from [Wells and Coppersmith \(1994\)](#) and [Moss and Ross \(2011\)](#). The 1989  
547 Ungava, Canada earthquake ([Adams et al., 1991](#)) also occurred in a non-extended  
548 craton and is included with the Australian events for our linear regression analysis.  
549 Regression equations are given in Fig. 6. For events of  $M_w < 7$ , the linear regression  
550 fitting shows that both the *MD* and *SRL* in non-extended cratonic areas are higher than  
551 global comparatives (Fig. 6). The large *SRL* for SCR earthquakes compared to  
552 analogous  $M_w$  global earthquakes is also reported by [Clark et al. \(2014\)](#).

553 [Wells and Coppersmith \(1994\)](#) found that the *SRL* is typically about 75% of  
554 subsurface rupture length. However, balancing  $M_w$  against *AD*, *L*, and shallow down-  
555 dip rupture width (i.e., rupture area), and considering aftershock distributions with  
556 respect to *SRL*, suggests  $SRL \approx$  subsurface rupture length in the Australian SCR  
557 earthquakes studied here. For example, the precisely located aftershocks of the  
558 Petermann earthquake enable mapping of a maximum sub-surface rupture length that  
559 is  $\approx SRL$  ([Attanayake et al., 2020](#)). This may be attributed to the shallow earthquake  
560 ruptures in bedrock that extend to the surface without significant influence of thin  
561 sediments.

562 Following our descriptions of fault stepovers, bends, and intersections above, we

563 compare the locations of observed *MD* against these fault geometric aspects. *MD* for  
564 the Petermann coincides with a fault stepover (Fig. 1, 2). *MD* for Pukatja, Lake Surprise  
565 East, Calingiri, Cadoux, and Lake Muir coincides with fault bends (Fig. 1, 2) and in the  
566 case of Pukatja and Calingiri, small step-overs in the rupture trace. *MD* for Meckering,  
567 and Marryat Creek coincides with fault intersections (Fig. 1, 2). Fault geometries in the  
568 regions of *MD* on the Kunayungku, Lake Surprise West, and Katanning surface ruptures  
569 can be considered sufficiently homogenous to not require classification into the  
570 geometric categories described above. In summary, *MD* occurs proximate to or directly  
571 within zones of enhanced fault geometric complexity (as evidenced from surface  
572 ruptures) in 8 of 11 earthquakes (73%), and *MD* can be approximated by  $3.3 \pm 1.6 (1\sigma)$   
573  $\times AD$ .

574

### 575 **Probability distribution of co-seismic slip**

576 The probability distribution of co-seismic slip is suggested to be a proxy of stress  
577 distribution and fault strength by [Thingbaijam and Mai \(2016\)](#), who undertook  
578 probability analysis by using sub-surface co-seismic slip data. Due to the limited dataset  
579 of surface co-seismic slip, especially for those earthquakes of  $M_w < 6$ , we only analyze  
580 the probability distribution of co-seismic slip for two endmember cases of Meckering  
581 and Petermann, for which the surface rupture geometry shows significant differences  
582 in distribution and shape (Fig. 1, 2).

583 With the uniformly sampled (0.1 km) co-seismic slip data, we first count the bins

584 of slip value in corresponding ranges; then measure the complementary cumulative  
585 distribution function ( $1 - F(u)$ ), which is fit by the exponential function,  $e^{-u/u_h}$ ,  
586 and the truncated exponential function,  $\frac{e^{-u/u_c} - e^{-u_{max}/u_c}}{1 - e^{-u_{max}/u_c}}$ , where  $u$  and  $u_{max}$  are  
587 the co-seismic slip and the maximum slip, respectively;  $u_h$  and  $u_c$  are the unknown  
588 rate parameters used in the regression for exponential function and truncated  
589 exponential function, respectively. In the case of the truncated exponential function, we  
590 also define  $u_t$  which denotes the position where the probabilities start to deviate from  
591 an exponential trend (Fig. 7). Both  $u_h$  and  $u_c$  are related to the expected value of the  
592 distribution, but  $u_c$  is likely to be larger than the maxima of the distribution, and the  
593 physical implications of different  $u_c$  is discussed later. The goodness of fit is measured  
594 by  $R^2$ .

595 The Meckering event is best fit by the truncated exponential function, while the  $R^2$   
596 is the same for both fitting functions in the case of Petermann earthquake (Fig. 7). The  
597 Meckering and Petermann cases represent two endmember cases listed in [Thingbaijam](#)  
598 [and Mai \(2016\)](#):  $u_c > u_t$  (subcritical behavior in Meckering where  $u_c$  is larger than  
599 the  $u_{max}$ , thus not shown in Fig. 7B) and  $u_c < u_t \approx u_{max}$  (near-critical behavior in  
600 Petermann where  $u_t$  is close to  $u_{max}$ , thus both fitting function produce close  $R^2$ ).  
601 These end members describe fault rupture propagation that has to overcome strong  
602 physical constraints during rupture (subcritical) versus weak physical impediments to  
603 rupture (near-critical).

604 The subcritical behavior observed for the Meckering event is suggestive of a  
605 spatially variable co-seismic stress drop (including relatively high and low components)

606 due to rupture on crustal structures that are variably-oriented with respect to  $S_{Hmax}$  (Fig.  
607 1, 8) and that require complex kinematic and geometric interactions to enable rupture  
608 propagation. This may ultimately favor a triangular shape for the slip distribution.  
609 Conversely, in the Petermann earthquake, the relatively straight, simple and ‘weak’  
610 source fault (related to inherited bedrock structure) and high-angle relationship with  
611 respect to  $S_{Hmax}$  and gravity gradient, may favor a more uniform displacement (low  
612 curvature) shape, albeit with localized complexity at a fault step-over (Fig. 1).

613

#### 614 **Comparison of rupture orientations with crustal geophysical properties**

615 Surface rupture traces are plotted on aeromagnetic intensity maps in Fig. 8 and on  
616 Bouguer gravity contour maps in Fig. 9. Additional rupture characteristics (stress drops  
617  $\Delta\sigma^s$ , discretized surface rupture orientations with respect to  $S_{Hmax}$ ) are shown in Fig. 10  
618 and compared to geophysical setting below.

619 All earthquakes similarly exhibit rupture traces that clearly align with prevailing  
620 magnetic structures (King et al., 2019). The Petermann earthquake surface rupture  
621 parallels the predominant NW-trending orientation of regional magnetic structure (Fig.  
622 8) and is parallel to NW-striking, NE-dipping bedrock foliations at the surface  
623 (Attanayake et al., 2020; King et al., 2019). Magnetic fabrics continue in rupture-  
624 parallel orientations beyond the rupture termini, although minor curvature is evident at  
625 the NW end; no high angle geophysical structures that could act as barriers to rupture  
626 are identified. The Pukatja surface rupture trace parallels the edge of a strong magnetic

627 contrast. The Marryat Creek ruptures are sub-parallel to E-W and NNE-trending  
628 lineament sets. The three Tennant Creek ruptures parallel NW and ~E-W lineaments,  
629 geological contacts, and previously mapped faults (Fig. 1C). The complex array of  
630 surface rupture traces in Cadoux parallel NW, NE, and E-W to ENE-WSW oriented  
631 magnetic fabrics. The northern and southern sections of the Meckering rupture parallel  
632 NE and NW-trending magnetic lineaments respectively; the central N-S striking rupture  
633 coincides with a less well defined but still identifiable zone of changes in magnetic  
634 structure and intensity. Katanning parallels NE-trending lineaments. The Calingiri  
635 rupture parallels N-trending lineaments (Fig. 8). [Clark et al. \(2019\)](#) conclude that the  
636 Lake Muir rupture trace parallels pre-existing structures evident as N to NE-trending  
637 surface features (valleys) that parallel minor lineament trends in the magnetic data; the  
638 bedrock structural controls on Lake Muir are amongst the least obvious in our dataset.

639 Of the total combined (summative) length of all surface ruptures (~148 km) we  
640 estimate between 133 km (90%) and 145 km (98%) aligns with geophysical structure  
641 in the host basement rocks (Fig. 8). In instances where one orientation of magnetic  
642 fabric is clearly dominant in the host bedrock (e.g., Petermann, southern part of Marryat  
643 Creek, all Tennant Creek earthquakes) the entire rupture trace is parallel to that fabric.  
644 Where two or three sets of magnetic fabrics are present, ruptures may involve all fabrics  
645 (e.g., Marryat Creek, Cadoux, Meckering) or remain confined to a single trace that is  
646 parallel to one fabric and truncated by distinct high-angle fabrics (e.g., Katanning,  
647 Calingiri).

648

649 **Type classification scheme for earthquakes based on crustal structure and rupture**  
650 **characteristics**

651 *Type 1*

652 The straightest (i.e., smallest range in incremental orientations; [Fig. 10A](#); classified  
653 as “*Type 1*” ruptures) and least segmented ruptures are the Petermann, Kunayungku,  
654 and Lake Surprise East ruptures. These *Type 1* ruptures all share the following  
655 characteristics: (1) the host bedrock contains a dominant bedrock fabric (e.g.,  
656 penetrative TMI fabric, surface geology foliations and faults) that is structurally  
657 continuous on the scale of surface ruptures (e.g., 10’s of km) and oriented  
658 perpendicular-to-high angle with respect to gravity gradients and  $S_{Hmax}$ ; (2) the average  
659 surface rupture trace is oriented approximately parallel to this bedrock fabric; (3)  
660 surface rupture traces have the lowest range of  $S_{Hmax}$  relative orientations ( $\sim 28^\circ$  to  $52^\circ$   
661 from  $S_{Hmax}$  perpendicular; [Fig. 10B](#) and inset) and are all oriented approximately  
662 perpendicular to the gravity gradient; (4) mean  $\Delta\sigma^s$  derived from ensemble models are  
663 average (e.g., Lake Surprise East) to low (e.g., Petermann) relative to the average from  
664 all earthquakes ([Fig. 10A](#)); (5) observed  $MD$  is in the central third of the ruptures ([Fig.](#)  
665 [2](#)); and (6) modeled displacement shapes are symmetric and lower amplitude, with a  
666 preference for elliptical shapes with centrally-located, modeled  $MD$  (ellipse apices, [Fig.](#)  
667 [2](#)) of similar value to  $AD$  (excluding Kunayungku).

668 The Petermann earthquake surface rupture is an example of *Type 1* earthquake. The  
669 rupture orientation is relatively straight ([Fig. 10B](#)) and oriented between  $27^\circ$  to  $47^\circ$   
670 (clockwise) from the normal of  $S_{Hmax}$  ([Fig. 8](#)). With a dip of  $\sim 30^\circ$  ([Attanayake et al.](#),

671 [2020](#)), the fault is thus well oriented for reverse-oblique faulting. The rupture source  
672 can be generally described as a fault that is sub-parallel to micaceous foliations in the  
673 hosting bedrock. Bedrock fabrics and the rupture trend between  $30 - 45^\circ$  from  $S_{Hmax}$   
674 perpendicular ([Rajabi et al., 2017](#)). Parallelism with bedrock fabrics is suggested to  
675 have enhanced rupture gliding and promoted a low stress drop rupture ([Attanayake et](#)  
676 [al., 2020](#)). The modeled  $MD$  for triangular and elliptical shapes is similar to the  $AD$   
677 (although the observed  $MD$  is  $\sim 7 AD$ ; [Fig. 2](#)). The critical behavior of the Petermann  
678 event observed in our probability distribution analysis of co-seismic slip indicates that  
679 this event had a relatively weak fault strength which results in a low amplitude elliptical  
680 to  $AD$  slip distribution. The rupture trace is orthogonal to the regional gravity gradient  
681 ([Fig. 9](#)) and thus stress perturbations that could result from geological density contrasts  
682 could enhance the propensity towards reverse slip. The mean  $\Delta\sigma^s$  derived from  
683 ensemble models of the Petermann earthquake ([Table S1](#)) is  $2.7 \pm 1.0$  ( $1 \sigma$ ) MPa; this  
684 is lower than the average  $\Delta\sigma^s$  from all earthquakes and is low compared to median stress  
685 drops from intraplate earthquakes globally ( $\sim 6$  MPa; [Allmann and Shearer \(2009\)](#)).

686

687 *Type 2*

688 *Type 2* crust contains multiple intersecting bedrock fabrics with varying  
689 orientations with respect to  $S_{Hmax}$  and gravity gradients, and no clearly dominant  
690 bedrock fabric at the scale of the individual rupture traces. *Type 2* ruptures (Katanning,  
691 Calingiri, Lake Surprise West, Marryat Creek, Pukatja, Meckering) exhibit surface  
692 rupture complexity, as evidenced by a large range of orientations relative to the



693 perpendicular of  $S_{Hmax}$  ( $0^\circ - 80^\circ$ ) and numerous stepped profiles in the cumulative *SRL*  
694 plot (Fig. 10B; Table S9). Highly misoriented (i.e., all traces  $>45$  to  $60^\circ$  with respect to  
695 the perpendicular of  $S_{Hmax}$ ) *Type 2* ruptures that are also influenced by surrounding high-  
696 angle structures (e.g., Lake Surprise W is bounded by Lake Surprise E and Kunayungku;  
697 Katanning is bounded by high angle geophysical lineaments; Fig. 8) exhibit the highest  
698 mean  $\Delta\sigma^s$  (Fig. 10A). Due to the high structural complexity of *Type 2* crust, *Type 2*  
699 ruptures exhibit the largest range in  $\Delta\sigma^s$ , including the lowest  $\Delta\sigma^s$  event (Marryat Creek;  
700 Fig. 10A), and the greatest diversity in orientations with respect to  $S_{Hmax}$  (e.g., Calingiri  
701 vs. Lake Surprise West).

702

703 *Type 3*

704 *Type 3* crust (locations of Lake Muir and Cadoux earthquakes) contains a dominant  
705 bedrock structure that is highly misaligned (i.e.  $< 20^\circ$ ) to  $S_{Hmax}$  and thus unfavorable for  
706 earthquake ruptures under the stress regime (see black arrows and dashed lineaments  
707 for Lake Muir and Cadoux in Fig. 8). Secondary structures include inherited faults and  
708 foliations that may be favorably or unfavorably oriented for brittle slip within active  
709 stress field. Gravity gradients may be highly oblique to  $S_{Hmax}$  (Fig. 9). Surface rupture  
710 geometries may be highly complex and variably oriented, particularly the Cadoux  
711 earthquake (Fig. 1, 10B); rupture traces tend to be more bimodally distributed into  
712 optimally ( $0-10^\circ$ ; Fig. 10B) and highly misoriented ( $> 60^\circ$ ; Fig. 10B) segments that  
713 reflect the interplay between extrinsic forcing by regional  $S_{Hmax}$  and the (misoriented)  
714 intrinsic structural properties of the host crust. This rupture type also exhibits the

715 highest overall degree of asymmetry in both modeled and observed *MD*. The preferred  
716 rupture shape is triangular, which we attribute to an increased distribution of off-fault  
717 damage associated with rupture propagation through structurally unfavorable host rock.  
718 Both *Type 3* events considered here are shallow, with very large *SRL:W* ratios (Fig. 2)  
719 and relatively low  $\Delta\sigma^s$  (Fig. 10A).

720 In terms of the Cadoux earthquake, the southern half of the surface rupture is  
721 primarily N-S oriented and well aligned with respect to  $S_{Hmax}$  for reverse faulting, while  
722 the northern half consists of a complex array of short E-W and N-S oriented rupture  
723 segments (Fig. 8). We posit this change in structural complexity may primarily reflect  
724 two aspects: (i) increasing abundance of misoriented penetrative E-W oriented  
725 structures to the north, which disrupt the N-S rupture and transfer slip across the  
726 complex fault array, and (ii) increasing influence of a large volume positive Bouguer  
727 anomaly to the north (indicated by circular contours in Fig. 9; also coincident with a  
728 zone of higher magnetic susceptibility on the TMI image in Fig. 8) that imparts a N-S  
729 gravity gradient that is approximately parallel to the average rupture trace orientation  
730 and is at a high angle to  $S_{Hmax}$ . We suggest the latter effects locally increase the  
731 proportional contribution of the secondary horizontal stress ( $\sigma_2$ ) relative to the regional  
732  $S_{Hmax}$  ( $\sigma_1$ ), therein increasing the potential for rupture transfer on to higher angle faults  
733 and overall rupture complexity. Local stress field rotations, including the possibility  
734 that the magnitude of the N-S oriented compressive stress locally exceeds the regional  
735  $S_{Hmax}$ , remain plausible hypotheses, collectively highlighting the potential for crustal  
736 structure to impart significant influence on rupture complexity. The slip asymmetry,

737 with *MD* towards the rupture terminus (Fig. 2), poor statistical fit to all functions and  
738 highly variable slip tapers at either end of the rupture (Fig. 3), abundant higher  
739 frequency displacement energy with embedded triangular slip shapes (Fig. 2, 4, 5) are  
740 additional characteristics of this rupture type.

741

## 742 **DISCUSSION**

### 743 **High-frequency slip maxima**

744 S-transform analysis reveals high-frequency ( $k > 10$ ) signals in four events that are  
745 spatially coincident with high spatial slip gradients ( $> 10^{-3}$ ) at fault stepovers  
746 (Petermann), bends (Calingiri, Lake Surprise East), and fault intersections (Cadoux).  
747 Stepovert widths on all faults are ubiquitously less than 2 km, consistent with empirical  
748 evidence for rupture propagation across  $< 2$  km-wide stepovers (Wesnousky, 2006,  
749 2008).

750 For a *Type I* rupture like Petermann, we suggest the observed high slip gradients  
751 and high-frequency signals at the steps are related to highly dynamic stress  
752 concentrations associated with rupture propagation across neighboring fault segments  
753 (Elliott et al., 2009; Oglesby, 2008). The threshold value of spatial slip gradient that  
754 permits rupture jump over gaps and stepovers was suggested to be  $> 2 \times 10^{-4}$ , which  
755 was based on the analysis of continental strike-slip earthquakes (Elliott et al., 2009).  
756 The observed spatial slip gradient in the Australian examples studied here is about one  
757 order of magnitude higher than the threshold value.

758 We note that the high slip gradient is only one aspect of the high-frequency signals;  
759 an abrupt increase and decrease of slip within several hundred meters is also observed.  
760 This short-wavelength feature is not predicted in the high stress concentration model  
761 ([Elliott et al., 2009](#); [Oglesby, 2008](#)) nor the theory of shallowly connected faults  
762 ([Oglesby, 2020](#)). It may relate to short-wavelength geological anomalies with lower  
763 shear modulus relating to lithologies that are cut by the fault ([Bürgmann et al., 1994](#)) or  
764 shallowly connected fault segments (e.g., en-echelon fracture networks) only hundreds  
765 of meters long ([Oglesby, 2020](#); [Quigley et al., 2012](#)). However, we do not find any  
766 evidence of lower shear modulus materials or short fault segments for these ruptures,  
767 based on examinations of geological and rupture maps, except for Cadoux (see next).

768 Zones of geometrically complicated interacting faults connected by opening  
769 fractures have been found elsewhere to produce the comparable high-frequency signal  
770 features to those observed here (e.g., see Fig. 9 in [Bürgmann et al. \(1994\)](#)). The linking  
771 fractures are able to transfer slip efficiently ([Bürgmann et al., 1994](#)). Fractures  
772 connecting fault bends and intersections were identified at Cadoux and Calingiri  
773 ([Gordon and Lewis, 1980](#); [Lewis et al., 1981](#)). The high-frequency signal in Marryat  
774 Creek is correlated to the fault junction zone where intersecting faults are orthogonally  
775 oriented with a wedge-shaped rupture geometry that can be considered kinematically  
776 and geometrically compatible. The mechanics of fault junctions suggests the  
777 intersection of these types of faults could act as earthquake nucleation points and foci  
778 of maximum slip ([Andrews, 1989](#)). If fault steps, bends, or high-angle fault  
779 intersections act as kinematic asperities, we might anticipate these to coincide with slip

780 maxima associated with maximum seismic energy release, and also high frequency  
781 variations in slip as variations in the intrinsic characteristics of the fault zone influence  
782 the dynamics of the propagating rupture.

### 783 **Slip taper and barriers**

784 Here we focus on the four events with slip taper  $> 10^{-3}$  that are considered outliers  
785 in [Fig. 3D](#). The high rupture tip taper value has been attributed elsewhere to (1) off-  
786 fault barriers of high frictional strength, (2) blocks of reduced shear modulus, (3)  
787 obliquely oriented structures, and (4) rupturing into a fault region that has previously  
788 experienced a large earthquake and is at a residual stress state ([Cappa et al., 2014](#);  
789 [Manighetti et al., 2004](#); [Perrin et al., 2016](#); [Scholz and Lawler, 2004](#)). The faults in  
790 Australian cratonic regions are considered immature or incipient faults (following  
791 definitions from ([Brodsky et al., 2011](#); [Perrin et al., 2016](#))). An absence of scarps in  
792 proximity to these historic ruptures suggests (4) is unlikely to account for the observed  
793 displacement patterns ([Clark et al., 2019](#); [Clark and McCue, 2003](#); [Crone et al., 2003](#)).

794 In this section, detailed structures are described for each surface-rupturing  
795 earthquake. The Calingiri event is asymmetric in slip distribution with a high rupture  
796 tip taper ( $1.2 \times 10^{-3}$ ) at the southern tip ([Fig. 3D](#); left end in [Fig. 2](#)). The southern tip is  
797 found to terminate at a nearly north-south striking lineament of low magnetic anomaly  
798 (dashed purple line in [Fig. 8](#)), while the whole rupture extends into a high-anomaly  
799 body, which sits on the hanging wall ([Fig. 8](#)).

800 The Pukatja event is 1.6 km long and has an asymmetric slip distribution with a

801 high rupture tip taper value ( $2.9 \times 10^{-3}$ ) at the eastern tip (Fig. 3D; right end in Fig. 2).  
802 The eastern tip stops at a lineament of high magnetic susceptibility while the other end  
803 (west) cuts into a body of relatively lower susceptibility (dash purple line in Fig. 8).  
804 The ends of other rupture tips of normal taper values (Fig. 3D) are not found to stop  
805 coincident with lineaments like those cases of high rupture tip taper values (Fig. 8).

806 The relatively high rupture tip taper in the right end (east) of Lake Surprise W and  
807 the left end (west) of Lake Surprise E (Fig. 3D) may be explained by the abrupt change  
808 of the dip direction of the hosting reverse fault (Fig. 1C) (Bowman, 1992; Mohammadi  
809 et al., 2019). The Lake Surprise W event ruptured a NE-dipping fault while the Lake  
810 Surprise E event ruptured a SW-dipping fault (Fig. 1B, 1C) (Bowman, 1992). For the  
811 high rupture tip taper of the right tip (east) of the Lake Surprise E event, referring to the  
812 1:250,000 Tennant Creek interpreted basement geology map (Johnston and Donnellan,  
813 2001), we find it stops at a location coincident with a fault separating volcanoclastic  
814 units from the undifferentiated granite (Fig. 1C).

815 These observations collectively suggest that obliquely orientated bedrock  
816 structures, identifiable as magnetic lineaments in geophysical data, coincide with the  
817 termini of some of the ruptures studied here, and can be associated with anomalously  
818 steep rupture tip tapers. No clear relationship is observed between tip taper steepness  
819 and prevailing rupture directivity, as proxied from estimates of epicentral location (Fig.  
820 2). The relationship between high rupture tip taper value and the presence of magnetic  
821 lineaments at high angles to the rupture plane provides evidence that obliquely oriented  
822 bedrock structures may be effective barriers to rupture propagation. Lineaments

823 orientated unfavorably to the rupture propagation direction may channel the  
824 propagating rupture into less efficient fracture pathways, therein dissipating fracture  
825 energy and terminating rupture propagation.

826 Through the study of structural control on rupture tip taper and the complexity of  
827 rupture segmentation, the role of pre-existing structures in facilitating or stopping  
828 rupture development is evident. The concept of rupture potential may provide some hint  
829 to the relations between earthquake initiation point and terminus point ([Weng and](#)  
830 [Ampuero, 2019](#)). The rupture potential theory suggests that final rupture termini are  
831 located at the places of the same rupture potential as that at the initiating position. The  
832 rupture potential theory determines the potential size of an earthquake provided that the  
833 spatial distribution of  $G_c/G_0$  is obtained, where  $G_c$  and  $G_0$  are the fracture energy  
834 and the steady state energy release rate, respectively. The fracture energy is a function  
835 of rupture acceleration, which is not available before the earthquake occurs, and may  
836 be obtained from some physical scaling, thus introducing large uncertainties.

837 Applying this theory to the Australian cratonic earthquakes, we find that where an  
838 initiating point is in the intersecting part of two faults, which had a high rupture  
839 potential, the earthquake would rupture through other intersecting segments. This forms  
840 complex rupture patterns as seen for the Meckering, Lake Muir, and Marryat Creek  
841 events. If the events initiated between two lineaments (dashed purple lines in [Fig. 8](#))  
842 and was of lower rupture potential than that of the intersection points, the final rupture  
843 would be limited by two lineaments. This forms relatively simple rupture patterns, like  
844 the Pukatja and Katanning events, where ruptures are located between two large

845 magnetic lineaments (dashed purple lines in Fig. 8). Therefore, the potential rupture  
846 length of a weak zone that is normal to the  $S_{Hmax}$  is controlled by two intersecting  
847 segments and is determined by the rupture potential of the initiating point.

848 In addition, the geophysical heterogeneity derived from the gravity map may reveal  
849 controlling factors on the Petermann earthquake, where no intersecting structure is  
850 detected through the TMI map. The gravity contours (marked by thick red lines in Fig.  
851 9), to the north-east of the surface rupture of the Petermann event, demonstrates a  
852 sudden offset (at the position P and P' in Fig. 9) from the general trend where it is  
853 coincident with the location of the rupture, which is dipping to the NE. This sudden  
854 change of gravity contours reflects a shallow high-density anomaly beneath the surface  
855 (Fig. 9). The size of this anomaly is comparable to the surface rupture length and may  
856 have controlled the length of the final rupture.

### 857 **Scaling between $MD$ , $SRL$ and $M_w$**

858 Fig. 6 demonstrates that Australian cratonic earthquakes have larger  $MD$  and longer  
859  $SRL$  than other earthquakes of comparable  $M_w$  (Wells and Coppersmith, 1994), with a  
860 few exceptions (e.g., Pukatja, Tennant Creek earthquakes in  $SRL$ ). The Australian  
861 earthquakes also predominate the subset of the global data with hypocenters shallower  
862 than 7 km depth (filled symbols). We note that the small sample size limits our  
863 confidence in whether the earthquakes studied here represent the expected range of  
864 surface-rupturing earthquake behaviours in cold and stable cratonic crust and we cannot  
865 dismiss possible effects of sampling bias. Nonetheless, we suggest that the shallowness



866 of Australian cratonic earthquakes, and their potential for lateral rupture propagation at  
867 shallow depths through highly fractured cratonic crust is expected to favour generation  
868 of higher  $SRL:W$  ratios and larger  $MD$  when compared to deeper, but otherwise  
869 similarly-sized, crustal earthquakes in the global datasets (e.g., [Wells and Coppersmith](#)  
870 [\(1994\)](#)). High  $SRL:W$  ratios are commonly observed in large earthquakes ( $M_w > 7$ )  
871 [\(Weng and Ampuero, 2019\)](#) where the rupture width is limited by regional brittle layer  
872 thickness. However, the shallowness and small rupture dimensions of the Australian  
873 cratonic earthquakes studied here preclude the involvement of ductile processes that  
874 limit the base of the rupture zone, such as enhanced viscous friction (e.g., [Schueller et](#)  
875 [al. \(2005\)](#)).

876 The Kunayungku, Lake Surprise E and Petermann earthquakes (*Type 1*; [Fig. 10](#))  
877 have simple surface rupture geometries with few definable segments or trend deviations  
878 ([Fig. S3](#), [Table S10](#)), but widely variable  $\Delta\sigma^s$  ([Fig. 10A](#); [Table S6](#)). We attribute this  
879 difference to the depth of the earthquake source. Our rupture width estimates for the  
880 Kunayungku and Lake Surprise East earthquakes range from 9.8 – 11.6 km ([Table S5](#)),  
881 while published estimates extend from the surface to depths of  $> 6$  km ([Choy and](#)  
882 [Bowman, 1990](#)) and up to 10 – 16 km ([Bowman, 1991](#); [Mohammadi et al., 2019](#)).  
883 InSAR inversion, CMT modelling and seismological analyses suggest the Petermann  
884 earthquake was limited to the top  $\sim 4$  km of the crust ([Attanayake et al., 2020](#); [Hejrani](#)  
885 [and Tkalčić, 2019](#); [Polcari et al., 2018](#)). The frictional strength of fault rocks in the  
886 shallow crust ( $< 5$  km) in cratonic areas is proposed to be much lower than deeper  
887 equivalents ([Bamford, 1976](#); [Denham et al., 1980](#)), and thus otherwise equivalent

888 ruptures channelled along highly anisotropic crustal weak zones (*Type I*) that extend to  
889 greater depths are hypothesized to have larger  $\Delta\sigma^s$  (Fig. 10).

890 We further speculate that increasing cratonic crustal strength with depth may inhibit  
891 downward rupture propagation via increasing fault friction and decreasing fracture  
892 continuity, whilst imposing a discernible effect on spectra of co-seismic slip  
893 distributions (Fig. 5B). For many earthquakes (e.g., Calingiri, Petermann) we find high  
894 energy concentrations at short wavelengths (1 to 5 km; Fig. 5) that are comparable with  
895 rupture widths. We envisage the rupture process to involve progressive energy bursts of  
896 propagating fractures with dimensions (e.g. diameters) set by the down-dip rupture  
897 width; these fractures coalesce to impart higher frequency displacement variations that  
898 are manifested as embedded shapes within the gross rupture profiles. These signals  
899 would be more discernible in shallower earthquakes and more attenuated in deeper  
900 earthquakes with smaller  $SRL:W$  ratios (e.g., Pukatja, Lake Surprise W).

901 This hypothesis is not incompatible with the large range of stress drops and rupture  
902 displacement shapes we observe in shallow cratonic earthquakes, as aspects such as co-  
903 seismic slip and rupture length could be highly dependent on shallow (< 5 km)  
904 variations in crustal structure, lithology, and other factors whilst still adhering to our  
905 hypothesis of depth-limited behaviour. The rupture of depth limited shallow  
906 earthquakes may be comparably less constrained from propagating laterally due to the  
907 presence of lithologic and structural heterogeneities that could enhance co-seismic  
908 rupture growth (Attanayake et al., 2020). Just as the lateral dimension of fault step-  
909 overs is important in limiting the size and mechanics of laterally propagating ruptures

910 ([Wesnousky, 2006](#)), perhaps variations in the strength (e.g., [Mooney et al. \(2012\)](#)) and  
911 stress distributions in cratonic crust favour depth partitioning of earthquakes with  
912 limited rupture widths. Our hypothesis also does not preclude the occurrence of deep  
913 cratonic earthquakes, such as the 1989 magnitude 5.6 Uluru earthquake (hypocentre  
914 depth = 31 km; [Michael-Leiba et al. \(1994\)](#)). Rather, we suggest the strength and  
915 strongly segmented nature of fractures in cratonic lithosphere could suppress upward  
916 propagation of deep earthquakes and downward propagation of shallow earthquakes,  
917 and thereby potentially limit earthquake maximum  $M_w$  in cratons (e.g., [Mooney et al.](#)  
918 [\(2012\)](#)).

#### 919 **Implications for seismic hazard: PFDHA inputs**

920 The principal aim of Probabilistic Fault Displacement Hazard Analysis (PFDHA)  
921 is to evaluate the potential for ground surface displacements of varying amounts, and  
922 across varying time-scales, associated with seismogenic fault rupture ([Moss and Ross,](#)  
923 [2011](#); [Youngs et al., 2003](#)). Empirical distributions for  $SRL$ ,  $MD$ ,  $AD$ , spatial variability  
924 of slip, and other statistical parameters are essential inputs into PFDHA calculations,  
925 which include probabilities of surface rupture at different  $M_w$  and slip exceedance  
926 distributions ([Moss and Ross, 2011](#)).

927 [Figure 11A](#) presents a new surface rupture probability curve for Australian cratonic  
928 earthquakes and compares this curve to prior curves from global regressions ([Moss and](#)  
929 [Ross, 2011](#)). Australian earthquake data was obtained for the period 1 January 1900 to  
930 21 October 2020 from Geoscience Australia's Earthquake Catalogue

931 (<https://earthquakes.ga.gov.au/>). We note that this earthquake catalogue does not  
932 include the revised  $M_W$  estimates from the 2018 National Seismic Hazard Assessment  
933 (NSHA18) ([Allen et al., 2018](#)) from which our surface rupture  $M_W$  values are sourced.  
934 However, the NSHA18 catalogue only extends to 2017 and excludes the Lake Muir  
935 earthquake. The earthquake catalogue was restricted to onshore Precambrian non-  
936 extended crust only ([Fig. 1](#)). We apply magnitude completeness cutoffs based on the  
937 Australian continent  $M_C$  estimates of [Allen et al. \(2018\)](#) ( $M_C 6.5 > 1920$ ;  $M_C 6.0 > 1920$ ;  
938  $M_C 4.5 > 1960$ ;  $M_C 4.0 > 1970$ ).

939 The percent of all earthquakes in each 0.1  $M_w$  increment that caused surface rupture  
940 are used as point data and fit by a regression curve with the logistic function following  
941 the method of [Moss and Ross \(2011\)](#). Six of nine Australian SCR earthquakes in this  
942 period with  $M_w \geq 6.0$  generated surface ruptures and thus the probability of surface  
943 rupture increases steeply over the  $6.0 \leq M_w \leq 6.5$  interval. Termination of the Australian  
944 SCR probability curve below 1.0 and at values of  $M_w > 6.6$  is intended to reflect  
945 epistemic uncertainty pertaining to the short historical seismologic record. Given the  
946 diverse nature of the reverse fault and Australian SCR curves, PFDHA could consider  
947 implementation of a logic tree weighted approach amongst these functions, depending  
948 upon the geological-seismological inputs and the desired conservativity of the analysis.  
949 As many deeper earthquakes in areas of enhanced sedimentary thickness contribute to  
950 the global regression, we favor weighting towards the SCR Oz curve (0.6 to 0.7) in  
951 Australian bedrock terrains.

952 [Figure 11B](#) compares observed  $AD$  and  $MD$  for the Australian earthquakes against

953 modelled  $AD$  and  $MD$  derived from regressions in the preminent PFDHA framework  
954 used to evaluate reverse faults ([Moss and Ross \(2011\)](#); equations in [Fig. 11](#) caption).  
955 Almost all Australia earthquakes have observed  $AD$  within  $\pm 30\%$  of the predicted  $AD$   
956 from [Moss and Ross \(2011\)](#) with the exception of the low slip, low stress drop  
957 Petermann earthquake ('P', [Fig. 11](#)). However, 9 of 11 Australian earthquakes have  
958 observed  $MD \gg$  modelled  $MD$  ( $> +30\%$  of predicted). We therefore calculate new  $AD$   
959 and  $MD$  to  $M_w$  linear regressions and present these in [Figure 11B](#). These formulae could  
960 be used or statistically preferred to other regressions (in a weighted logic tree content)  
961 for PFDHAs in SCR bedrock regions.

962 In terms of displacement profiles, eight of eleven earthquakes (73%) have observed  
963  $MD$  in the central third of the rupture ([Fig. 2](#)) and seven of eleven earthquakes (64%)  
964 have 'symmetric' best-fitting functions ([Fig. 3C](#); [Table S2](#)). Although a flat line fit  
965 (displacement at any given point along the rupture is equal to  $AD$ ) is not the preferred  
966 shape for any events, it produces close results (i.e.,  $AD \approx$  modeled  $MD$ ) to the best fit  
967 in Petermann and Lake Surprise E. Incremental displacements along a specified fault  
968 in a *Type 1* setting ([Fig. 10](#)) could thus be appropriately modelled using  $AD$  estimates  
969 obtained from the scaling relationship in [Fig. 11B](#). From the perspective of PFDHA  
970 however, it is difficult to accurately forecast the shape and symmetry of surface rupture  
971 displacement fields for future earthquakes across a diverse range of SCR settings. To  
972 resolve this, we normalize incremental displacements ( $D$ ) against  $AD$  at fault positions  
973 ( $x$ ) against  $SRL$  for all rupture types. The  $x$  axis is the rupture half length, with each  
974 rupture yielding two data points for each displacement increment. We fit a mean

975 regression and  $1\sigma$  error bounds to all data (Fig. 11C).

976 Fig. 11C shows  $D$  is  $\leq AD$  within the first 10% of the *SRL* (measured from either  
977 rupture tip) and  $D \geq AD$  within the middle 80% of the rupture (0.2 to 0.5). The highest  
978 values of  $D$  (i.e.,  $> AD$ ) and lowest uncertainty bounds are observed in the middle  
979 quintile of the rupture. *Type 2* and *3* faults exhibit the largest variability along the  
980 rupture trace (i.e.,  $D/AD > 1\sigma$  bounds). The largest  $1\sigma$  incremental  $D/AD$  occur in the  
981 first 20% of the rupture length. PFDHA practitioners could consider the structural-  
982 geophysical setting type (Fig. 10) with these data (Fig. 11) to select conservative bounds  
983 for incremental PFDHA estimates depending upon the location of a site along a rupture  
984 trace. At the simplest level, the mean curve and  $1\sigma$  bounds presented in Fig. 11C could  
985 represent a reasonable approximation of  $D/AD$  irrespective of geological setting.

986 As a final demonstration of how the results of this study could inform PFDHA, we  
987 show gamma probability distribution functions (PDFs) for  $D / AD$  at fixed values of  $x$   
988 / *SRL* ranging from the first 5% of the surface rupture ( $x / SRL = 0.05$ ) to the rupture  
989 mid-point ( $x / SRL = 0.5$ ). PDFs shift to higher proportionate values of  $D / AD$  towards  
990 the rupture mid-point (i.e.,  $D > AD$ ), but retain strong probability distributions of  $D <$   
991  $AD$  at all locations.

## 992 CONCLUSIONS

- 993 1.  $AD : MD$  ratios range from 0.13 (Petermann earthquake) to 0.67 (Katanning) with  
994 a mean of  $0.36 \pm 0.14$  ( $1\sigma$ ). Of the 8 ruptures analyzed, 50% exhibit unilateral and  
995 50% exhibit bilateral rupture directivity. If the observed and modelled positions of

996 *MD* relative to *SRL* are combined, approximately 68% of earthquakes have *MD* in  
997 the middle third of the rupture and 16% each of the end thirds.

998 2. Surface co-seismic slip distributions for the studied earthquakes generally adhere  
999 to asymmetric triangular or elliptical shapes, but there is not a preferred shape for  
1000 all events studied here. There are two prevailing endmember forms of co-seismic  
1001 along-strike slip distribution: the low curvature to rectangular shape (e.g.,  
1002 Petermann; close to an elliptical shape) for earthquakes with a roughly straight and  
1003 localized damage zone (*Type I* structures) and the higher curvature shape (e.g.,  
1004 Meckering; close to a triangular shape) for earthquakes with complex segmented  
1005 surface rupture geometries. The latter is proposed to originate from higher  
1006 frictional stress on the fault plane relative to the former and may include intensive  
1007 off-fault damage zones. Crustal structure plays an important role in rupture  
1008 characteristics.

1009 3. S-transform analysis on the residuals suggests that while basic shapes may be  
1010 representative of the slip distributions there are significant contributions in the form  
1011 of high spatial frequency (short-wavelength) signals that we attribute to factors that  
1012 influence the rupture process, including stress concentrations coincident with fault  
1013 geometric complexities (e.g., stepovers or intersections) and depth controls on the  
1014 rupture source (e.g., shallow earthquakes exhibit high frequency displacement  
1015 variations with wavelengths similar to rupture width).

1016 4. The higher value of *MD* and *SRL* in Australia compared to global examples may  
1017 be attributed to the shallow earthquake hypocenters in the former data (mean 3.6

1018  $\pm 1.9$  km). Shallow earthquakes are expected to be more likely to have SRL  $\approx$   
1019 subsurface rupture length, AD  $\approx$  subsurface AD, and MD  $\approx$  subsurface MD.  
1020 Enhanced stress concentrations at geometrically compatible fault junctions (e.g.,  
1021 Marryat Creek) may further increase MD.

1022 5. Surface rupture geometries are controlled by bedrock fabrics, which are mainly  
1023 revealed by the TMI map. Of the total combined (summative) length of all surface  
1024 ruptures (~148 km), we estimate between 133 km (90%) and 145 km (98%) aligns  
1025 with geophysical structure in the host basement rocks. The host bedrock contains a  
1026 dominant bedrock fabric that is structurally continuous in the scale of surface  
1027 ruptures (e.g., 10's of km) and oriented perpendicular-to-high angle with respect to  
1028 gravity gradients and  $S_{Hmax}$  tend to produce relatively simple and straight surface  
1029 rupture (*Type 1*; e.g. Petermann). If the bedrock fabrics consists of intersected  
1030 segments with variable orientations in the scale that is comparable to the surface  
1031 rupture length, it tends to produce complex surface ruptures (*Type2* and *Type3*; e.g.,  
1032 Meckering and Cadoux). At the scale of this study, we are unable to determine  
1033 whether TMI fabric geometries truly parallel rupture geometries in three  
1034 dimensions, or are simply aligned in trace; if only the latter is true, TMI fabrics  
1035 may play more alternative roles in enhancing rupture propagation (e.g, fluid  
1036 conduits) rather than simply providing zones of enhanced frictional weakness.

1037 6. New  $\Delta\sigma^s$  estimates are derived based on published estimates and three methods  
1038 incorporating  $W$ ,  $M_0$ ,  $AD$ , and  $\mu$ . The average stress drop for all earthquakes is  $4.8$   
1039  $\pm 2.8$  ( $1 \sigma$ ).  $\Delta\sigma^s$  derived from ensemble models for the *Type 1* and *Type 3*



1040 earthquakes are close to or lower than the average from all earthquakes, and *Type*  
1041 2 earthquakes has large variations in  $\Delta\sigma^s$ .

1042 7. The rupture tip taper value at the termini is consistent with the result from global  
1043 database and compliments existing data in slip mode. The asymmetry of  
1044 displacement distribution and extremely steep rupture tip tapers are found to be  
1045 affected by bedrock fabrics obliquely oriented with respect to the rupture strike.

1046 8. The interaction between regional  $S_{Hmax}$ , intersecting segments, and the gravity  
1047 gradient, increases surface rupture complexity (e.g., the Cadoux event). The  
1048 segment length of a magnetic lineament that is normal to  $S_{Hmax}$  may set the limit of  
1049 an earthquake surface rupture by intersecting other lineaments at low angle ( $< 45^\circ$ )  
1050 to the  $S_{Hmax}$ .

1051 9. *MD* are commonly (8 of 11 earthquakes; 73%) located coincident with fault steps,  
1052 bends, and/or high-angle fault intersections. S-transform analysis reveals that the  
1053 spike-like high-frequency slip maxima also coincide with fault steps and junctions,  
1054 suggesting concentrations of hierarchical fractal fault damage networks embedded  
1055 within areas of geometric and kinematic incompatibility. The geometric  
1056 compatibility or incompatibility of fault intersection zones provides a fruitful  
1057 avenue for future research. It is clear from this study that fault intersections should  
1058 not be simply treated as converging areas where displacement tapers to net-zero  
1059 slip in seismic hazard. In some cases, fault geometric complexities could be  
1060 forecasted to have slip maxima; this is particularly important to consider in  
1061 probabilistic fault displacement seismic hazard analyses for critical infrastructure.

1062 10. The earthquakes in Australian SCRs have a higher surface rupture probability at  
1063  $M_w > 5.7$  than predicted from prior reverse fault regression curves, necessitating  
1064 consideration of additional surface rupture probability functions in PFDHA.  
1065 Incremental surface displacements increase to approximately  $AD$  within the first  
1066 10% of the  $SRL$  (measured from either rupture tip) and  $D_{is} \geq AD$  within the middle  
1067 80% of the rupture.

1068

## 1069 **ACKNOWLEDGEMENTS**

1070 We would like to acknowledge the Noongar people of south-west Western Australia,  
1071 the Warumungu people of Tennant Creek, and the Antakirinja, Yankunytjatjara, and  
1072 Pitjantjatjara people of the Western Desert and APY lands in South Australia / Northern  
1073 Territory, as the traditional custodians of the land on which all historic surface ruptures  
1074 occurred, and where the data described in this paper were collected. This research was  
1075 funded by the Australian Research Council through Discovery Grant #DP170103350 to  
1076 M. Quigley. We acknowledge the support of Dan Clark and Trevor Allen from  
1077 Geoscience Australia towards enhancing our knowledge of Australian earthquakes. T.  
1078 King received support from the David Hay Postgraduate Writing-Up Award (University  
1079 of Melbourne). H. Yang received the Melbourne Research Scholarship, the  
1080 Baragwanath Travel Scholarship and the Albert Shimmins Writing-Up Award from the  
1081 University of Melbourne to assist in research development. Geophysical maps are  
1082 produced by using the Generic Mapping Tools (GMT) package ([Wessel et al., 2013](#)).

- 1084 Adams, J., Wetmiller, R. J., Hasegawa, H. S., and Drysdale, J., 1991, The first surface  
1085 faulting from a historical intraplate earthquake in North America: *Nature*, v. 352,  
1086 no. 6336, p. 617-619.
- 1087 Allen, T., Leonard, M., Ghasemi, H., and Gibson, G., 2018, The 2018 National Seismic  
1088 Hazard Assessment: Earthquake epicentre catalogue (GA Record 2018/30).  
1089 Geoscience Australia, Commonwealth of Australia, Canberra, ACT.
- 1090 Allmann, B. P., and Shearer, P. M., 2009, Global variations of stress drop for moderate  
1091 to large earthquakes: *Journal of Geophysical Research-Solid Earth*, v. 114, no.  
1092 B1.
- 1093 Andrews, D. J., 1989, Mechanics of Fault Junctions: *Journal of Geophysical Research-*  
1094 *Solid Earth and Planets*, v. 94, no. B7, p. 9389-9397.
- 1095 Attanayake, J., King, T. R., Quigley, M. C., Gibson, G., Clark, D., Jones, A. G.,  
1096 Brennand, S. L., and Sandiford, M., 2020, Rupture Characteristics and Bedrock  
1097 Structural Control of the 2016 M w 6.0 Intraplate Earthquake in the Petermann  
1098 Ranges, Australia: *Bulletin of the Seismological Society of America*.
- 1099 Bamford, W. E., 1976, Evolution of stresses in rock masses, as related to compressive  
1100 strengths and plate tectonics: *Investigation of Stress in Rock: Advances in Stress*  
1101 *Measurement; Preprints of Papers*, p. 63.
- 1102 Bowman, J. R., 1991, Geodetic Evidence for Conjugate Faulting during the 1988  
1103 Tennant Creek, Australia Earthquake Sequence: *Geophysical Journal*

1104 International, v. 107, no. 1, p. 47-56.

1105 -, 1992, The 1988 Tennant Creek, Northern Territory, Earthquakes - a Synthesis:  
1106 Australian Journal of Earth Sciences, v. 39, no. 5, p. 651-669.

1107 Brodsky, E. E., Gilchrist, J. J., Sagy, A., and Collettini, C., 2011, Faults smooth  
1108 gradually as a function of slip: Earth and Planetary Science Letters, v. 302, no.  
1109 1-2, p. 185-193.

1110 Brown, S. R., and Scholz, C. H., 1985, Broad Bandwidth Study of the Topography of  
1111 Natural Rock Surfaces: Journal of Geophysical Research-Solid Earth and  
1112 Planets, v. 90, no. B14, p. 2575-2582.

1113 Bürgmann, R., Pollard, D. D., and Martel, S. J., 1994, Slip distributions on faults:  
1114 effects of stress gradients, inelastic deformation, heterogeneous host-rock  
1115 stiffness, and fault interaction: Journal of Structural Geology, v. 16, no. 12, p.  
1116 1675-1690.

1117 Cappa, F., Perrin, C., Manighetti, I., and Delor, E., 2014, Off-fault long-term damage:  
1118 A condition to account for generic, triangular earthquake slip profiles:  
1119 Geochemistry, Geophysics, Geosystems, v. 15, no. 4, p. 1476-1493.

1120 Choy, G. L., and Bowman, J. R., 1990, Rupture process of a multiple main shock  
1121 sequence: analysis of teleseismic, local, and field observations of the Tennant  
1122 Creek, Australia, earthquakes of January 22, 1988: Journal of Geophysical  
1123 Research: Solid Earth, v. 95, no. B5, p. 6867-6882.

1124 Clark, D., Brennand, S., Brenn, G., Allen, T., Garthwaite, M., and Standen, S., 2019,  
1125 The 2018 Lake Muir earthquake sequence, southwest Western Australia:

1126 rethinking Australian stable continental region earthquakes: *Solid Earth*.

1127 Clark, D., and McCue, K., 2003, Australian paleoseismology: towards a better basis for  
1128 seismic hazard estimation: *Annals of Geophysics*, v. 46, no. 5, p. 1087-1105.

1129 Clark, D., McPherson, A., Allen, T., and De Kool, M., 2014, Coseismic Surface  
1130 Deformation Caused by the 23 March 2012 M-w 5.4 Ernabella (Pukatja)  
1131 Earthquake, Central Australia: Implications for Fault Scaling Relations in  
1132 Cratonic Settings: *Bulletin of the Seismological Society of America*, v. 104, no.  
1133 1, p. 24-39.

1134 Clark, D., McPherson, A., and Van Dissen, R., 2012, Long-term behaviour of Australian  
1135 stable continental region (SCR) faults: *Tectonophysics*, v. 566, p. 1-30.

1136 Cowie, P. A., and Scholz, C. H., 1992a, Growth of Faults by Accumulation of Seismic  
1137 Slip: *Journal of Geophysical Research-Solid Earth*, v. 97, no. B7, p. 11085-  
1138 11095.

1139 -, 1992b, Physical Explanation for the Displacement Length Relationship of Faults  
1140 Using a Post-Yield Fracture-Mechanics Model: *Journal of Structural Geology*,  
1141 v. 14, no. 10, p. 1133-1148.

1142 Crone, A. J., De Martini, P. M., Machette, M. N., Okumura, K., and Prescott, J. R., 2003,  
1143 Paleoseismicity of two historically quiescent faults in Australia: Implications  
1144 for fault behavior in stable continental regions: *Bulletin of the Seismological*  
1145 *Society of America*, v. 93, no. 5, p. 1913-1934.

1146 Dawson, J., Cummins, P., Tregoning, P., and Leonard, M., 2008, Shallow intraplate  
1147 earthquakes in Western Australia observed by Interferometric Synthetic

1148 Aperture Radar: *Journal of Geophysical Research-Solid Earth*, v. 113, no. B11.

1149 Denham, D., 1988, Australian seismicity-the puzzle of the not so stable continent:  
1150 *Seismological Research Letters*, v. 59, no. 4, p. 235-240.

1151 Denham, D., Alexander, L. G., Everingham, I. B., Gregson, P. J., Mccaffrey, R., and  
1152 Enever, J. R., 1987, The 1979 Cadoux Earthquake and Intraplate Stress in  
1153 Western-Australia: *Australian Journal of Earth Sciences*, v. 34, no. 4, p. 507-  
1154 521.

1155 Denham, D., Alexander, L. G., and Worotnicki, G., 1980, The stress field near the sites  
1156 of the Meckering (1968) and Calingiri (1970) earthquakes, Western Australia:  
1157 *Tectonophysics*, v. 67, no. 3-4, p. 283-317.

1158 Dentith, M., Clark, D., and Featherstone, W., 2009, Aeromagnetic mapping of  
1159 Precambrian geological structures that controlled the 1968 Meckering  
1160 earthquake (Ms 6.8): Implications for intraplate seismicity in Western Australia:  
1161 *Tectonophysics*, v. 475, no. 3-4, p. 544-553.

1162 Dentith, M. C., Dent, V. F., and Drummond, B. J., 2000, Deep crustal structure in the  
1163 southwestern Yilgarn Craton, Western Australia: *Tectonophysics*, v. 325, no. 3-  
1164 4, p. 227-255.

1165 Dolan, J. F., and Haravitch, B. D., 2014, How well do surface slip measurements track  
1166 slip at depth in large strike-slip earthquakes? The importance of fault structural  
1167 maturity in controlling on-fault slip versus off-fault surface deformation: *Earth  
1168 and Planetary Science Letters*, v. 388, p. 38-47.

1169 Elliott, A. J., Dolan, J. F., and Oglesby, D. D., 2009, Evidence from coseismic slip

1170 gradients for dynamic control on rupture propagation and arrest through  
1171 stepovers: *Journal of Geophysical Research-Solid Earth*, v. 114, no. B2.

1172 Frankel, A., 1991, High-frequency spectral falloff of earthquakes, fractal dimension of  
1173 complex rupture, b value, and the scaling of strength on faults: *Journal of*  
1174 *Geophysical Research: Solid Earth*, v. 96, no. B4, p. 6291-6302.

1175 Gabriellov, A., Keilis-Borok, V., and Jackson, D. D., 1996, Geometric incompatibility  
1176 in a fault system: *Proc Natl Acad Sci U S A*, v. 93, no. 9, p. 3838-3842.

1177 Gold, R. D., Reitman, N. G., Briggs, R. W., Barnhart, W. D., Hayes, G. P., and Wilson,  
1178 E., 2015, On-and off-fault deformation associated with the September 2013 Mw  
1179 7.7 Balochistan earthquake: Implications for geologic slip rate measurements:  
1180 *Tectonophysics*, v. 660, p. 65-78.

1181 Gordon, F. R., and Lewis, J. D., 1980, The Meckering and Calingiri earthquakes  
1182 October 1968 and March 1970.

1183 Griffith, W. A., Di Toro, G., Pennacchioni, G., Pollard, D. D., and Nielsen, S., 2009,  
1184 Static stress drop associated with brittle slip events on exhumed faults: *Journal*  
1185 *of Geophysical Research: Solid Earth*, v. 114, no. B2.

1186 Haeussler, P. J., Schwartz, D. P., Dawson, T. E., Stenner, H. D., Lienkaemper, J. J.,  
1187 Sherrod, B., Cinti, F. R., Montone, P., Craw, P. A., Crone, A. J., and Personius,  
1188 S. F., 2004, Surface rupture and slip distribution of the Denali and Totschunda  
1189 faults in the 3 November 2002 M 7.9 earthquake, Alaska: *Bulletin of the*  
1190 *Seismological Society of America*, v. 94, no. 6, p. S23-S52.

1191 Hejrani, B., and Tkalčić, H., 2019, The 20 May 2016 Petermann Ranges earthquake:

1192 centroid location, magnitude and focal mechanism from full waveform  
1193 modelling: Australian Journal of Earth Sciences, v. 66, no. 1, p. 37-45.

1194 Huang, Y., Ellsworth, W. L., and Beroza, G. C., 2017, Stress drops of induced and  
1195 tectonic earthquakes in the central United States are indistinguishable: Sci Adv,  
1196 v. 3, no. 8, p. e1700772.

1197 Johnston, A., and Donnellan, N., 2001, Tennant Creek 1:250 000 Integrated  
1198 Interpretation of Geophysics and Mapped Geology: Northern Territory  
1199 Geological Survey, Alice Springs, Australia, scale 1:250 000.

1200 Johnston, A. C., 1989, The seismicity of 'stable continental interiors', Earthquakes at  
1201 North-Atlantic passive margins: Neotectonics and postglacial rebound, Springer,  
1202 p. 299-327.

1203 Kaneko, Y., and Fialko, Y., 2011, Shallow slip deficit due to large strike-slip  
1204 earthquakes in dynamic rupture simulations with elasto-plastic off-fault  
1205 response: Geophysical Journal International, v. 186, no. 3, p. 1389-1403.

1206 King, G., 1983, The Accommodation of Large Strains in the Upper Lithosphere of the  
1207 Earth and Other Solids by Self-Similar Fault Systems - the Geometrical Origin  
1208 of B-Value: Pure and Applied Geophysics, v. 121, no. 5-6, p. 761-815.

1209 King, T. R., Quigley, M., and Clark, D., 2019, Surface-Rupturing Historical  
1210 Earthquakes in Australia and Their Environmental Effects: New Insights from  
1211 Re-Analyses of Observational Data: Geosciences, v. 9, no. 10, p. 408.

1212 King, T. R., Quigley, M. C., and Clark, D., 2018, Earthquake environmental effects  
1213 produced by the Mw 6.1, 20th May 2016 Petermann earthquake, Australia:



1214 Tectonophysics, v. 747, p. 357-372.

1215 Klinger, Y., 2010, Relation between continental strike-slip earthquake segmentation  
1216 and thickness of the crust: *Journal of Geophysical Research: Solid Earth*, v. 115,  
1217 no. B7.

1218 Leonard, M., 2008, One hundred years of earthquake recording in Australia: *Bulletin*  
1219 *of the Seismological Society of America*, v. 98, no. 3, p. 1458-1470.

1220 -, 2010, Earthquake Fault Scaling: Self-Consistent Relating of Rupture Length, Width,  
1221 Average Displacement, and Moment Release: *Bulletin of the Seismological*  
1222 *Society of America*, v. 100, no. 5a, p. 1971-1988.

1223 Leonard, M., Burbidge, D., Allen, T., Robinson, D., McPherson, A., Clark, D., and  
1224 Collins, C., 2014, The challenges of probabilistic seismic-hazard assessment in  
1225 stable continental interiors: An Australian example: *Bulletin of the*  
1226 *Seismological Society of America*, v. 104, no. 6, p. 3008-3028.

1227 Lewis, J. D., Daetwyler, N. A., Bunting, J. A., and Moncrieff, J. S., 1981, The Cadoux  
1228 earthquake, Western Australia: *Geol. Surv. Rept*, v. 11, p. 133.

1229 Madariaga, R., 1977, Implications of stress-drop models of earthquakes for the  
1230 inversion of stress drop from seismic observations, *Stress in the Earth*, Springer,  
1231 p. 301-316.

1232 Mai, P. M., and Beroza, G. C., 2002, A spatial random field model to characterize  
1233 complexity in earthquake slip: *Journal of Geophysical Research-Solid Earth*, v.  
1234 107, no. B11, p. ESE 10-11-ESE 10-21.

1235 Manighetti, I., King, G., and Sammis, C. G., 2004, The role of off-fault damage in the

1236 evolution of normal faults: *Earth and Planetary Science Letters*, v. 217, no. 3-4,  
1237 p. 399-408.

1238 Manighetti, I., Zigone, D., Campillo, M., and Cotton, F., 2009, Self-similarity of the  
1239 largest-scale segmentation of the faults: Implications for earthquake behavior:  
1240 *Earth and Planetary Science Letters*, v. 288, no. 3-4, p. 370-381.

1241 McCue, K., Barlow, B. C., Denham, D., Jones, T., Gibson, G., and Michael-Leiba, M.,  
1242 1987, Another chip off the old Australian block: *Eos, Transactions American*  
1243 *Geophysical Union*, v. 68, no. 26, p. 609-612.

1244 McGill, S. F., and Rubin, C. M., 1999, Surficial slip distribution on the central Emerson  
1245 fault during the June 28, 1992, Landers earthquake, California: *Journal of*  
1246 *Geophysical Research-Solid Earth*, v. 104, no. B3, p. 4811-4833.

1247 Michael-Leiba, M., Love, D., McCue, K., and Gibson, G., 1994, The Uluru (Ayers  
1248 Rock), Australia, earthquake of 28 May 1989: *Bulletin of the Seismological*  
1249 *Society of America*, v. 84, no. 1, p. 209-214.

1250 Mohammadi, H., Quigley, M., Steacy, S., and Duffy, B., 2019, Effects of source model  
1251 variations on Coulomb stress analyses of a multi-fault intraplate earthquake  
1252 sequence: *Tectonophysics*, v. 766, p. 151-166.

1253 Mooney, W. D., Ritsema, J., and Hwang, Y. K., 2012, Crustal seismicity and the  
1254 earthquake catalog maximum moment magnitude ( $M_{\text{cmax}}$ ) in stable continental  
1255 regions (SCRs): Correlation with the seismic velocity of the lithosphere: *Earth*  
1256 *and planetary science letters*, v. 357, p. 78-83.

1257 Moss, R. E. S., and Ross, Z. E., 2011, Probabilistic Fault Displacement Hazard Analysis

1258 for Reverse Faults: Bulletin of the Seismological Society of America, v. 101, no.  
1259 4, p. 1542-1553.

1260 Oglesby, D., 2008, Rupture termination and jump on parallel offset faults: Bulletin of  
1261 the Seismological Society of America, v. 98, no. 1, p. 440-447.

1262 Oglesby, D. D., 2020, What Can Surface - Slip Distributions Tell Us about Fault  
1263 Connectivity at Depth?: Bulletin of the Seismological Society of America.

1264 Okubo, P. G., and Aki, K., 1987, Fractal geometry in the San Andreas fault system:  
1265 Journal of Geophysical Research: Solid Earth, v. 92, no. B1, p. 345-355.

1266 Perrin, C., Manighetti, I., Ampuero, J. P., Cappa, F., and Gaudemer, Y., 2016, Location  
1267 of largest earthquake slip and fast rupture controlled by along -strike change in  
1268 fault structural maturity due to fault growth: Journal of Geophysical Research:  
1269 Solid Earth, v. 121, no. 5, p. 3666-3685.

1270 Polcari, M., Albano, M., Atzori, S., Bignami, C., and Stramondo, S., 2018, The  
1271 causative fault of the 2016 Mw 6.1 Petermann ranges intraplate earthquake  
1272 (Central Australia) retrieved by C-and L-band InSAR data: Remote Sensing, v.  
1273 10, no. 8, p. 1311.

1274 Power, W. L., and Tullis, T. E., 1991, Euclidean and Fractal Models for the Description  
1275 of Rock Surface-Roughness: Journal of Geophysical Research-Solid Earth and  
1276 Planets, v. 96, no. B1, p. 415-424.

1277 Quigley, M., Mohammadi, H., and Duffy, B., 2017, Multi-fault earthquakes with  
1278 kinematic and geometric rupture complexity: how common: INQUA Focus  
1279 Group Earthquake Geology and Seismic Hazards.

1280 Quigley, M., Van Dissen, R., Litchfield, N., Villamor, P., Duffy, B., Barrell, D., Furlong,  
1281 K. P., Stahl, T., Bilderback, E., and Noble, D., 2012, Surface rupture during the  
1282 2010 Mw 7.1 Darfield (Canterbury) earthquake: Implications for fault rupture  
1283 dynamics and seismic-hazard analysis: *Geology*, v. 40, no. 1, p. 55-58.

1284 Rajabi, M., Tingay, M., Heidbach, O., Hillis, R., and Reynolds, S., 2017, The present-  
1285 day stress field of Australia: *Earth-Science Reviews*, v. 168, p. 165-189.

1286 Scholz, C. H., and Lawler, T. M., 2004, Slip tapers at the tips of faults and earthquake  
1287 ruptures: *Geophysical Research Letters*, v. 31, no. 21.

1288 Schueller, S., Gueydan, F., and Davy, P., 2005, Brittle-ductile coupling: Role of ductile  
1289 viscosity on brittle fracturing: *Geophysical Research Letters*, v. 32, no. 10.

1290 Segall, P., and Pollard, D. D., 1980, Mechanics of Discontinuous Faults: *Journal of*  
1291 *Geophysical Research*, v. 85, no. Nb8, p. 4337-4350.

1292 Shen, Z. K., Sun, J. B., Zhang, P. Z., Wan, Y. G., Wang, M., Burgmann, R., Zeng, Y. H.,  
1293 Gan, W. J., Liao, H., and Wang, Q. L., 2009, Slip maxima at fault junctions and  
1294 rupturing of barriers during the 2008 Wenchuan earthquake: *Nature Geoscience*,  
1295 v. 2, no. 10, p. 718-724.

1296 Starr, A. T., Slip in a crystal and rupture in a solid due to shear, *in* *Proceedings*  
1297 *Mathematical Proceedings of the Cambridge Philosophical Society* 1928,  
1298 Volume 24, Cambridge University Press, p. 489-500.

1299 Stirling, M., McVerry, G., Gerstenberger, M., Litchfield, N., Van Dissen, R., Berryman,  
1300 K., Barnes, P., Wallace, L., Villamor, P., Langridge, R., Lamarche, G., Nodder,  
1301 S., Reyners, M., Bradley, B., Rhoades, D., Smith, W., Nicol, A., Pettinga, J.,

1302 Clark, K., and Jacobs, K., 2012, National Seismic Hazard Model for New  
1303 Zealand: 2010 Update: Bulletin of the Seismological Society of America, v. 102,  
1304 no. 4, p. 1514-1542.

1305 Stockwell, R. G., Mansinha, L., and Lowe, R. P., 1996, Localization of the complex  
1306 spectrum: The S transform: Ieee Transactions on Signal Processing, v. 44, no. 4,  
1307 p. 998-1001.

1308 Thingbaijam, K. K. S., and Mai, P. M., 2016, Evidence for Truncated Exponential  
1309 Probability Distribution of Earthquake Slip: Bulletin of the Seismological  
1310 Society of America, v. 106, no. 4, p. 1802-1816.

1311 Wells, D. L., and Coppersmith, K. J., 1994, New Empirical Relationships among  
1312 Magnitude, Rupture Length, Rupture Width, Rupture Area, and Surface  
1313 Displacement: Bulletin of the Seismological Society of America, v. 84, no. 4, p.  
1314 974-1002.

1315 Weng, H. H., and Ampuero, J. P., 2019, The Dynamics of Elongated Earthquake  
1316 Ruptures: Journal of Geophysical Research-Solid Earth, v. 124, no. 8, p. 8584-  
1317 8610.

1318 Weng, H. H., and Yang, H. F., 2017, Seismogenic width controls aspect ratios of  
1319 earthquake ruptures: Geophysical Research Letters, v. 44, no. 6, p. 2725-2732.

1320 Wesnousky, S. G., 2006, Predicting the endpoints of earthquake ruptures: Nature, v. 444,  
1321 no. 7117, p. 358-360.

1322 -, 2008, Displacement and geometrical characteristics of earthquake surface ruptures:  
1323 Issues and implications for seismic-hazard analysis and the process of

1324 earthquake rupture: Bulletin of the Seismological Society of America, v. 98, no.  
1325 4, p. 1609-1632.

1326 Wessel, P., Smith, W., Scharroo, R., Luis, J., and Wobbe, F., 2013, Generic mapping  
1327 tools: improved version released: Eos, Transactions American Geophysical  
1328 Union, v. 94, no. 45, p. 409-410.

1329 Youngs, R. R., Arabasz, W. J., Anderson, R. E., Ramelli, A. R., Ake, J. P., Slemmons,  
1330 D. B., McCalpin, J. P., Doser, D. I., Fridrich, C. J., Swan, F. H., Rogers, A. M.,  
1331 Yount, J. C., Anderson, L. W., Smith, K. D., Bruhn, R. L., Knuepfer, P. L. K.,  
1332 Smith, R. B., dePolo, C. M., O'Leary, D. W., Coppersmith, K. J., Pezzopane, S.  
1333 K., Schwartz, D. P., Whitney, J. W., Olig, S. S., and Toro, G. R., 2003, A  
1334 methodology for probabilistic fault displacement hazard analysis (PFDHA):  
1335 Earthquake Spectra, v. 19, no. 1, p. 191-219.

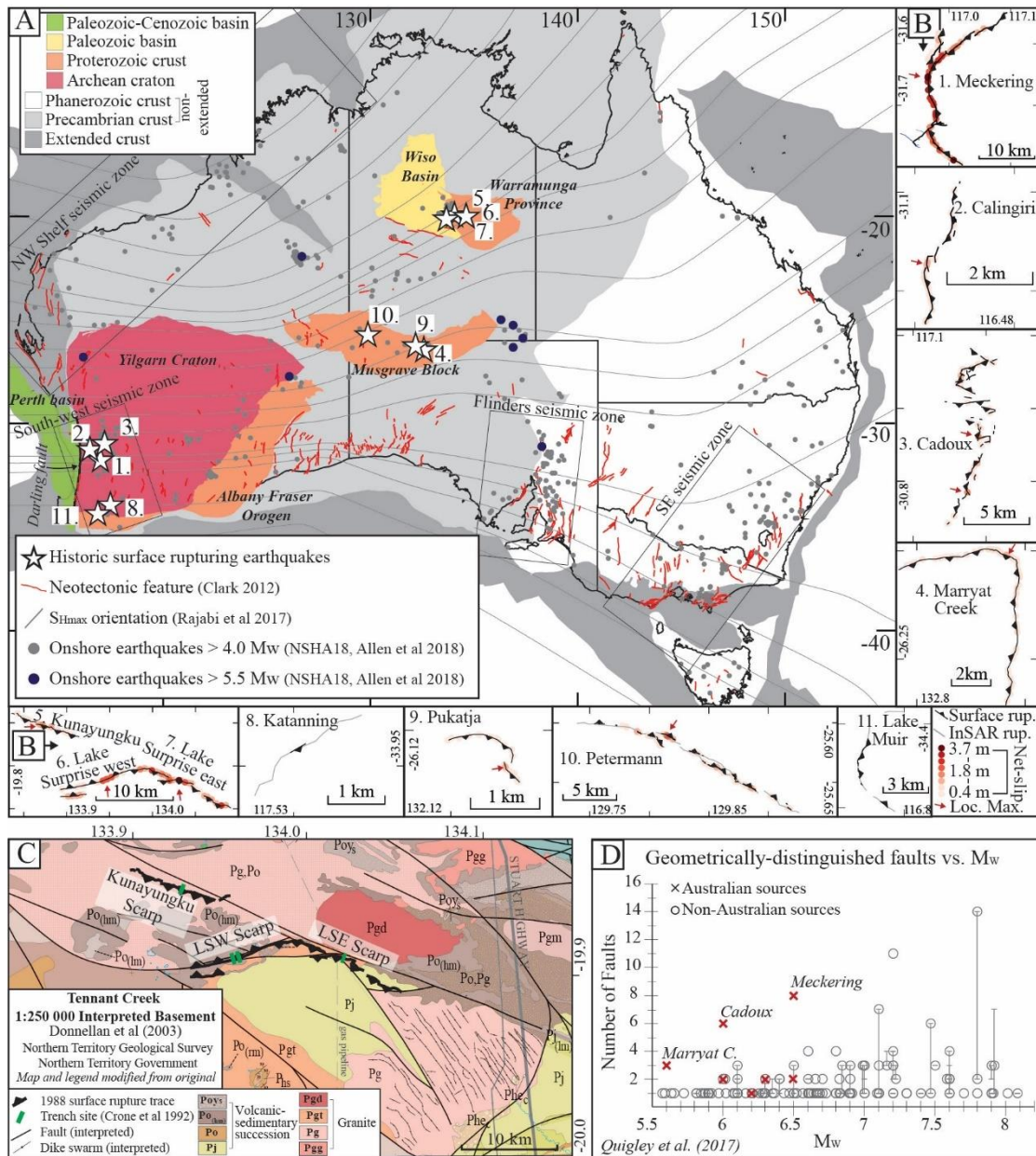
1336 Zhao, S., and Muller, R. D., 2003, Three-dimensional finite-element modelling of the  
1337 tectonic stress field in continental Australia: SPECIAL PAPERS-  
1338 GEOLOGICAL SOCIETY OF AMERICA, v. 372, p. 71.

1339 Zielke, O., Klinger, Y., and Arrowsmith, J. R., 2015, Fault slip and earthquake  
1340 recurrence along strike-slip faults—Contributions of high-resolution  
1341 geomorphic data: Tectonophysics, v. 638, p. 43-62.

1342 Zinke, R., Hollingsworth, J., and Dolan, J. F., 2014, Surface slip and off - fault  
1343 deformation patterns in the 2013 MW 7.7 Balochistan, Pakistan earthquake:  
1344 Implications for controls on the distribution of near-surface coseismic slip:  
1345 Geochemistry, Geophysics, Geosystems, v. 15, no. 12, p. 5034-5050.

1346

1347

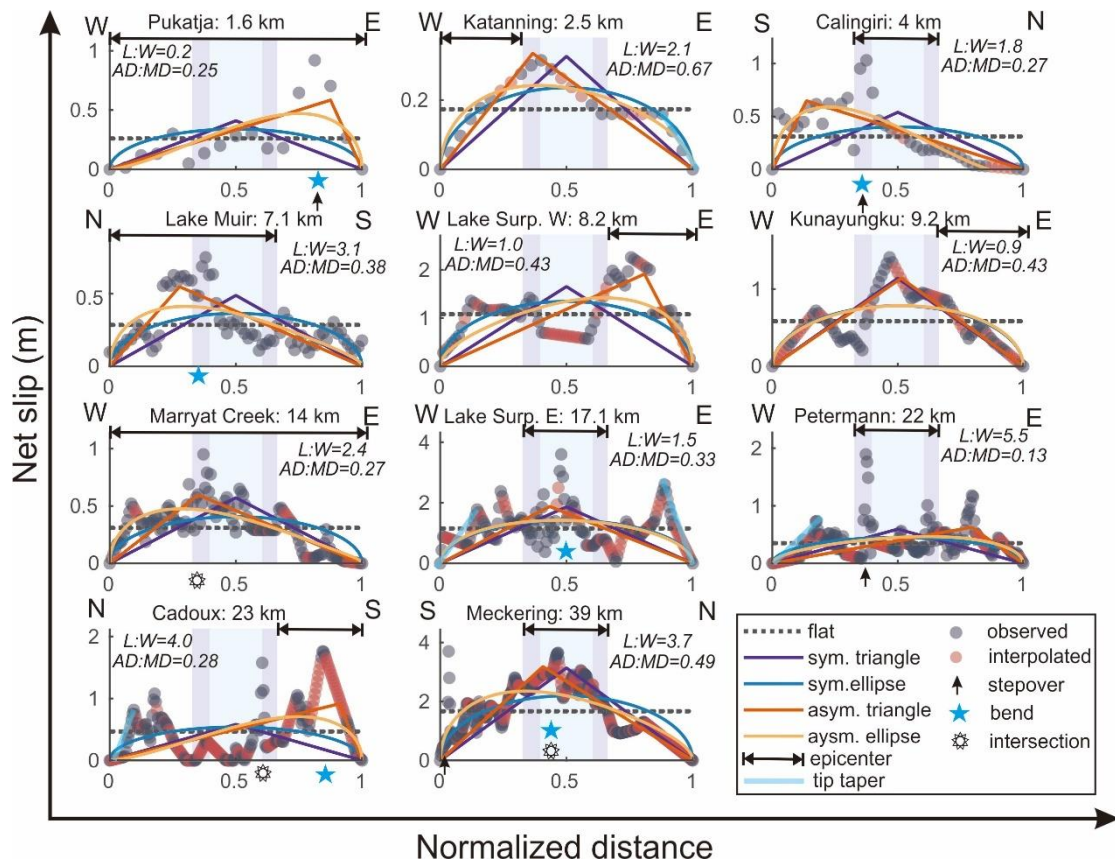


1349

1350 **Figure 1.** (A) Map of Australia showing sites of historic surface-rupturing  
 1351 earthquakes, geological provinces (Leonard et al., 2014), onshore historic earthquakes >  
 1352 4.0 (1840 – 2017) (Allen et al., 2018), crustal stress trajectory (Rajabi et al., 2017),  
 1353 neotectonic features (<http://pid.geoscience.gov.au/dataset/ga/74056>) and seismic zones  
 1354 (Leonard, 2008). The four rectangular boxes mark four high seismicity zones in



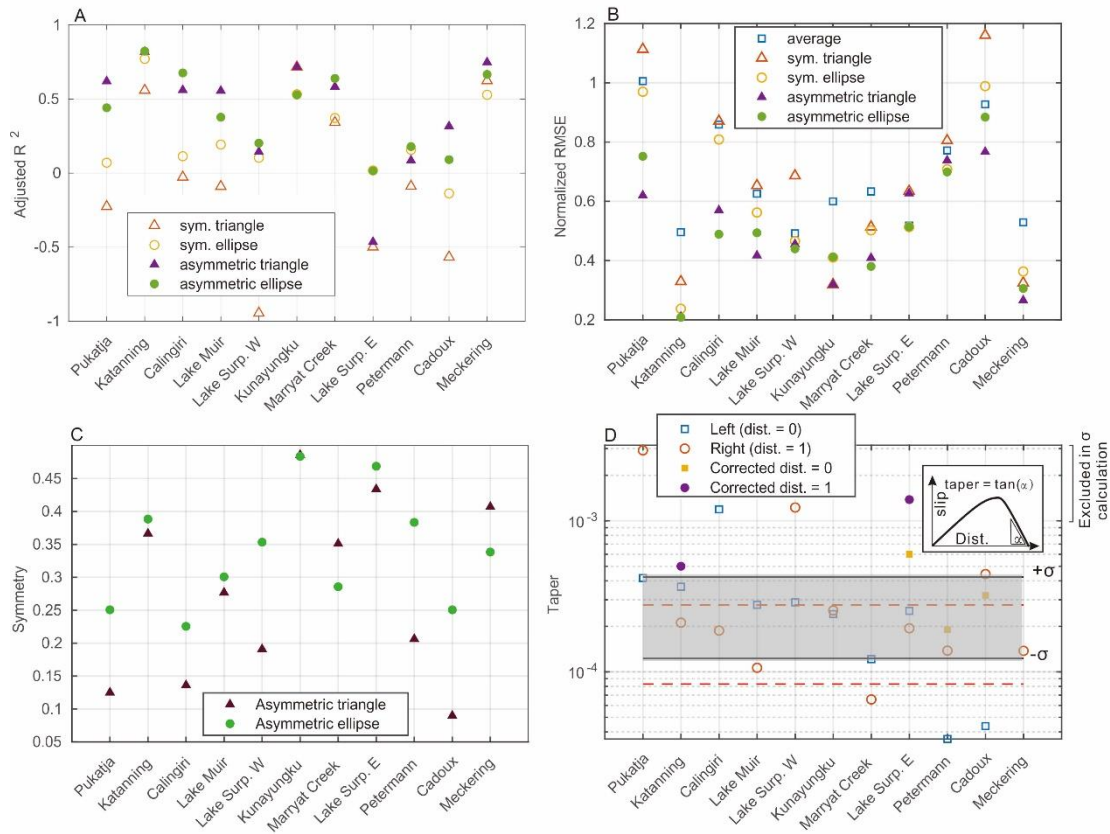
1355 Australia. (B) Maps of surface rupture for each event, numbered chronologically. Dots  
1356 demonstrate the position of original field measurements, and the color code notes the  
1357 amount of net slip. Small red arrows note the location of slip maxima for each event.  
1358 (C) Interpreted bedrock geology surrounding the Tennant Creek events. The ruptures  
1359 are aligned with local structures. The legend is simplified to focus on the structures  
1360 around the surface rupture, for more details refer to [Johnston and Donnellan \(2001\)](#). (D)  
1361 The geometric complexity of rupture segmentation versus the magnitude. The surface-  
1362 rupturing earthquakes ( $M_w > 5.5$ ) in Australia are plotted against global compilations  
1363 ([Quigley et al. 2017](#)). The bars denote segmentation ranges of multi-fault earthquakes  
1364 based on all reported studies.  
1365



1366

1367 **Figure 2.** Best-fitting regression curves of different regular shapes to the 11 co-  
 1368 seismic displacement profiles in Australian SCRs. The events are ordered by rupture  
 1369 length. The distance to the start point is normalized to the rupture length, which is  
 1370 labeled after the name of each event in the title. The filled circles represent the  
 1371 resampled data points. The red color means the resampled point has no original  
 1372 observations within 200 m while the grey ones indicate the nearest interpolation  
 1373 distance is < 200 m. The central quintile ( $x = 0.4 - 0.6$ ) and central third ( $x = 0.33 -$   
 1374  $0.67$ ) are represented by the faint blue and pink box, respectively. The location of the  
 1375 preferred range of seismic derived epicenters in each area are projected to fault plane.  
 1376 The epicenter ranges roughly mark the relative position of sources with respect to the  
 1377 central third of the profile. A range across the whole profile means we cannot put any

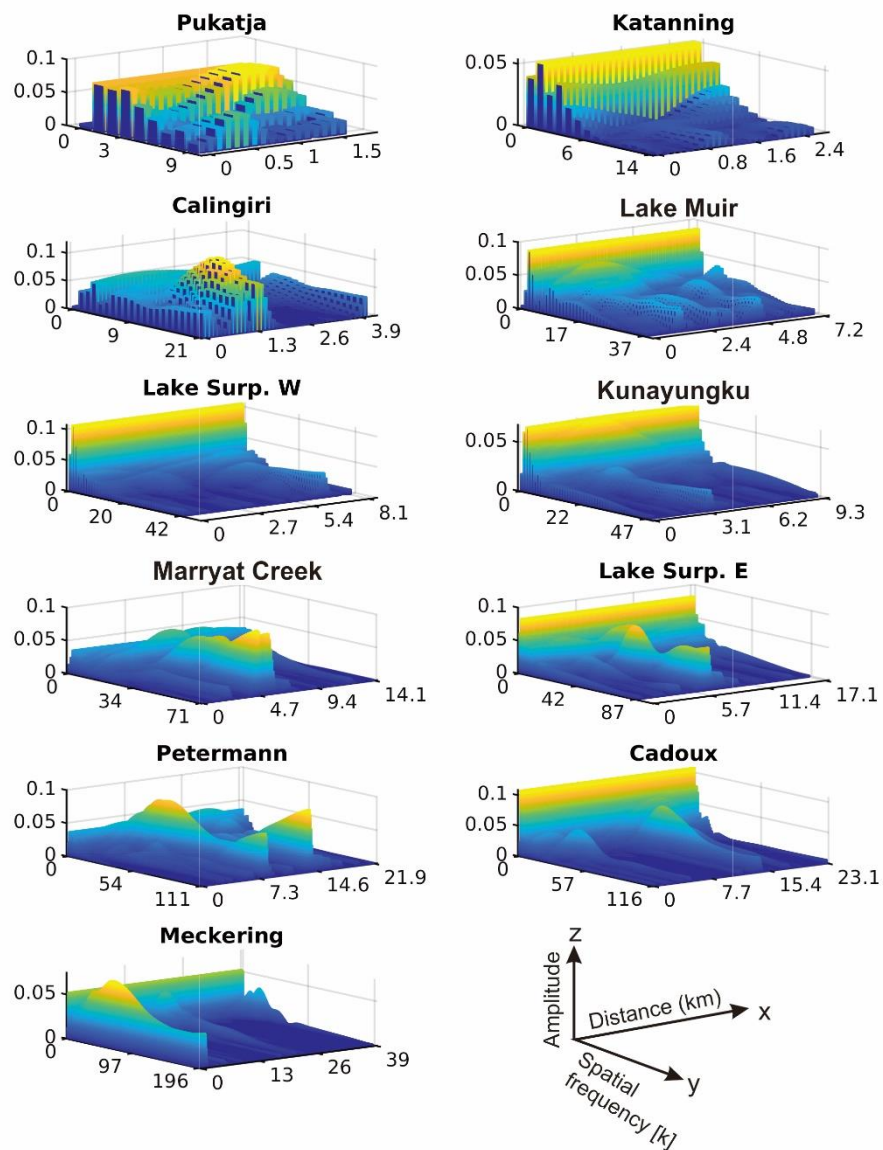
1378 preferred range for corresponding event according to the reported data and uncertainties.  
1379 The black arrow marks the position of the slip maxima that has the high spatial  
1380 frequency in net slip (abrupt rise and drop in few hundred meters) coincident with fault  
1381 stepovers, blue star coincident with fault junctions. For the slip taper calculation, we  
1382 first use the asymmetric triangular shape function, which may over smooth the slip  
1383 profile where there are strong perturbations. We correct those taper angle calculations  
1384 at ending segments. The thick blue lines are corrections for the rupture tip taper  
1385 calculation for those ending segments. The rupture length ( $L$ ):width ( $W$ ) ratios and  
1386 average displacement ( $AD$ ) : maximum displacement ( $MD$ ) ratios are reported for each  
1387 event. Stress drops (in MPa) reported from the literature ('observed'; see text for  
1388 sources) and modelled from a logarithmic regression fit to per unit area data ('*modelled*';  
1389 see text for details) are: Pukatja (3.7), Katanning (20.5, 9.0), Calingiri (9.0, 6.0), Lake  
1390 Muir (3.3), Lake Surprise West (13.0, 9.5), Kunayungku (5.8, 3.8), Marryat Creek (1.5),  
1391 Lake Surprise East (8.6, 5.9), Petermann (2.2, 2.7), Cadoux (2.0, 2.4), Meckering (9.0,  
1392 4.9) (Table S1, S6).  
1393



1394

1395 **Figure 3.** Post-analysis of the fitting results of different shapes. (A) adjusted  $R^2$  for  
 1396 each shape function regression of all events to evaluate the goodness of the fitting. The  
 1397 higher  $R^2$ , the better fitting result. (B) The root-mean-square error (RMSE) is  
 1398 normalized by the mean value of corresponding measurements. (C) Symmetry for each  
 1399 event. (D) The rupture tip taper for each event. The insert sketch illustrates the  
 1400 calculation of rupture tip taper, which is defined as the spatial slip gradient when it  
 1401 approaches the terminus. The marked grey area within two black lines shows  $1\sigma$   
 1402 perturbations of the data (exclude 4 outliers of value  $> 10^{-3}$ ). The perturbation within  
 1403 two red dash lines are existing dataset for long (>30 – 100s km) ruptures of strike-slip  
 1404 or normal fault mechanisms (Scholz and Lawler, 2004). Data for each subplot are  
 1405 included in Table S2.

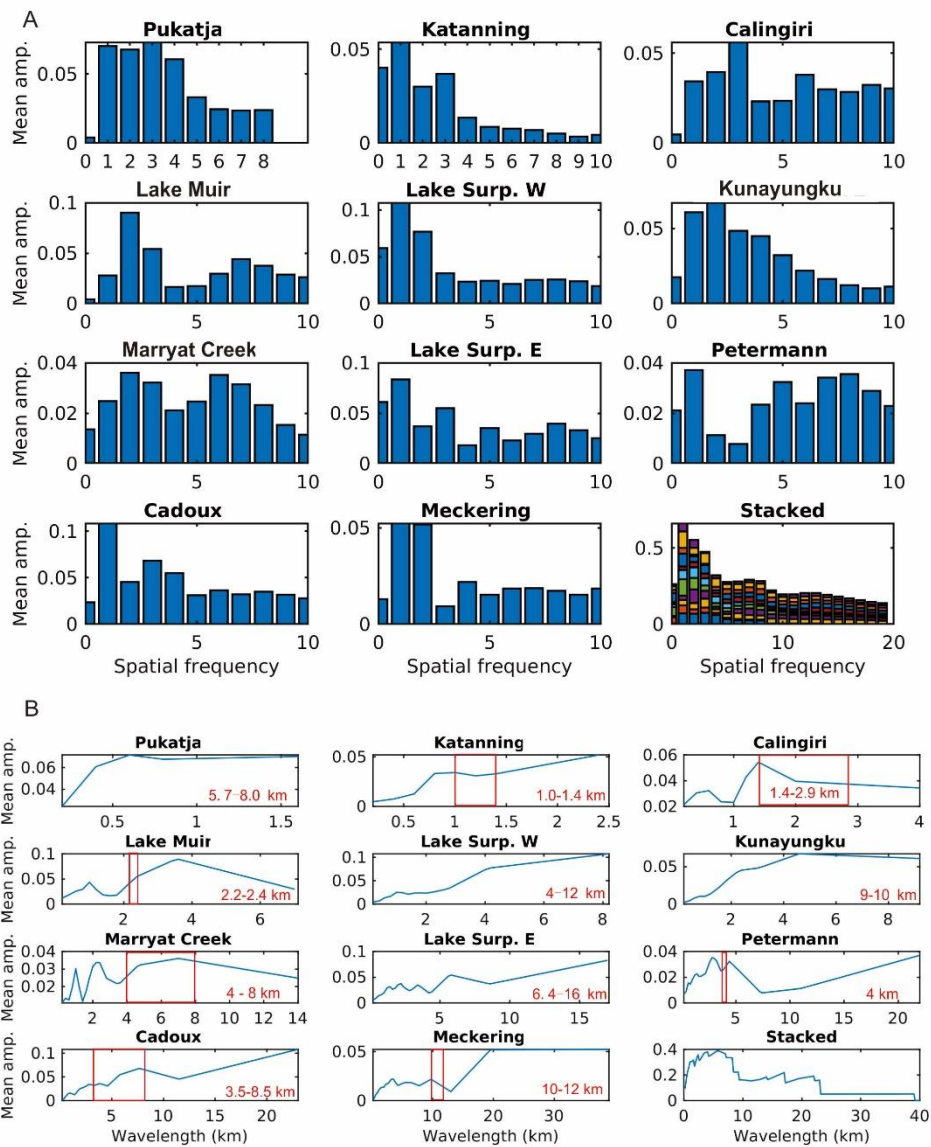




1407

1408 **Figure 4.** S-transform analyses for the residuals of the best-fitting regression  
 1409 curves for different shapes. The dominating spatial frequency is generally less than 5,  
 1410 but there are significant high-frequency signals for Calingiri (at  $x \sim 1.3$  km), Marryat  
 1411 Creek (at  $x \sim 5$  km), Lake Surprise East (at  $x \sim 7$  km), Petermann (at  $x \sim 8$  km),  
 1412 Cadoux (at  $x \sim 14$  km).

1413

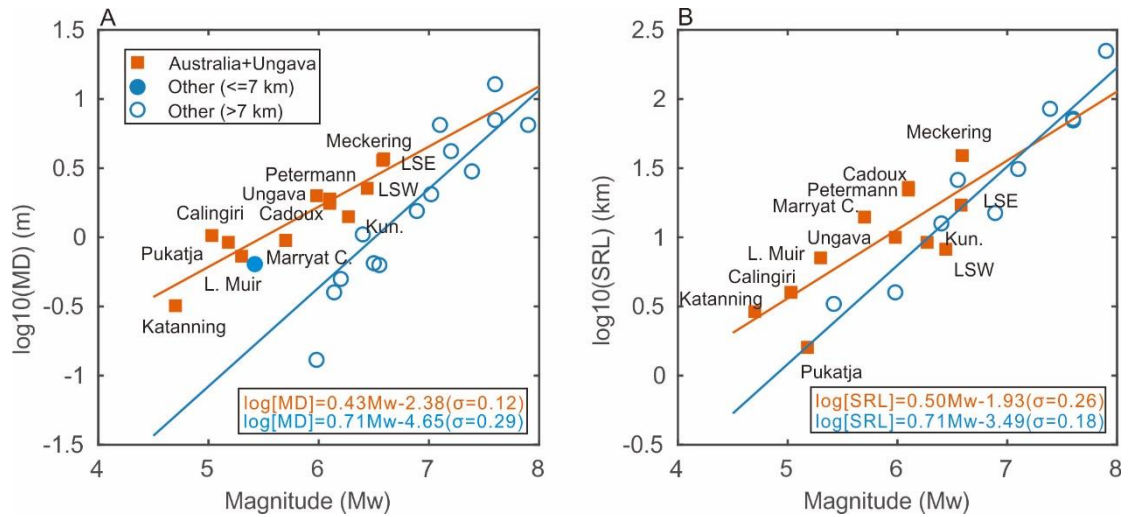


1414

1415 **Figure 5.** Averaging amplitude of the S-transform results versus the spatial  
 1416 frequency (A) and wavelength (B) over the whole domain for each event. (A) Only  
 1417 those spatial frequency lower than 10 are shown here as the averaging method would  
 1418 smooth out those high spatial frequency signals and the mean amplitude quickly  
 1419 decreases with spatial frequency after the dominating spatial frequency (i.e., 1-3),  
 1420 especially for the stacked case. (B) The spatial frequency is converted to the  
 1421 wavelength with the rupture length. The down-dip rupture width is noted for each

1422 event and is also marked with a red box in x-axis for those events with  $SRL:W > 1$ .  
1423 The mean amplitude of the S-transform results generally decreases with the  
1424 wavelength, but some events have large contributions from short-wavelength signals  
1425 ( $< \sim 5$  km), which are comparable with the down-dip rupture width for those relatively  
1426 shallow events.  
1427

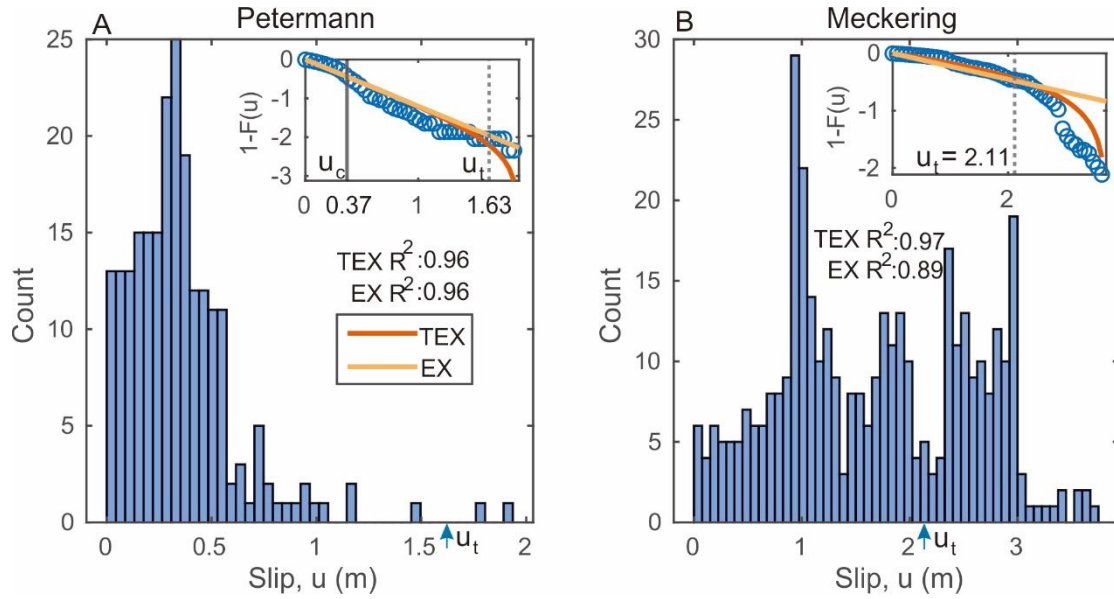




1428

1429 **Figure 6.** Comparison of the maximum slip (A) and rupture length (B) versus  
 1430 magnitude scaling relationship for thrust earthquakes between non-extended cratons  
 1431 in Australia and Ungava (Canada) and other areas ([Moss and Ross, 2011](#); [Wells and](#)  
 1432 [Coppersmith, 1994](#)). The solid lines correspond to the linear regression results for the  
 1433 two groups. The value of slip maxima and rupture length in Australia is estimated to  
 1434 be higher than global comparatives.

1435



1437

1438 **Figure 7.** Histograms of the co-seismic slip for the Peterman (A) and Meckering

1439 (B) earthquakes. The insert plot shows the complementary cumulative distribution

1440 function  $(1 - F(u))$ , which are fit by exponential functions (EX) and truncated

1441 exponential functions (TEX). The fitting result is measured by  $R^2$ . The Petermann

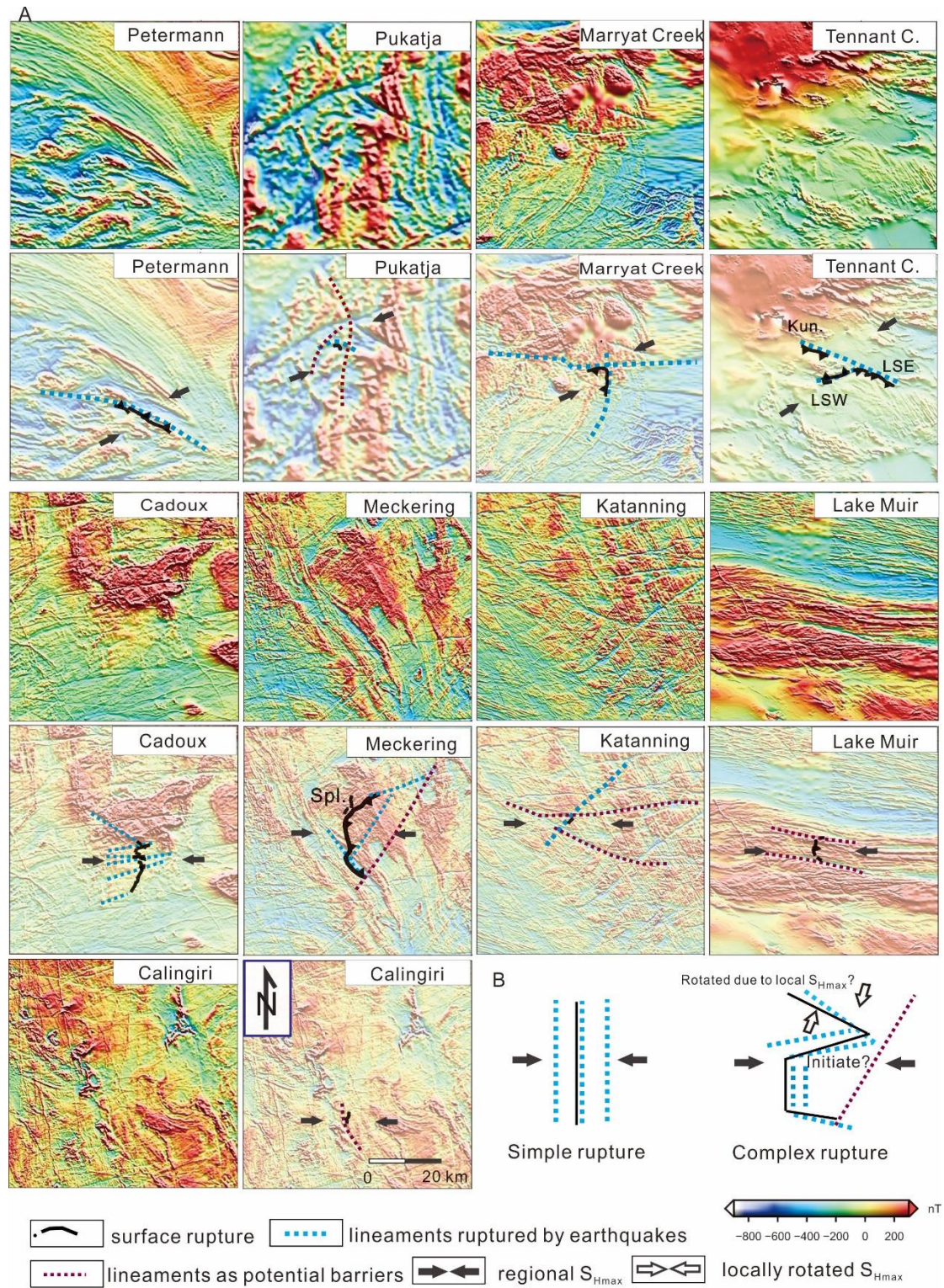
1442 earthquake demonstrates a near-critical behavior, while the Meckering earthquake a

1443 sub-critical behavior.  $u_h$  and  $u_c$  are the unknown rate parameters in regression. In

1444 the case of the truncated exponential function,  $u_t$  is the position where the

1445 probabilities start to deviate from an exponential trend.

1446

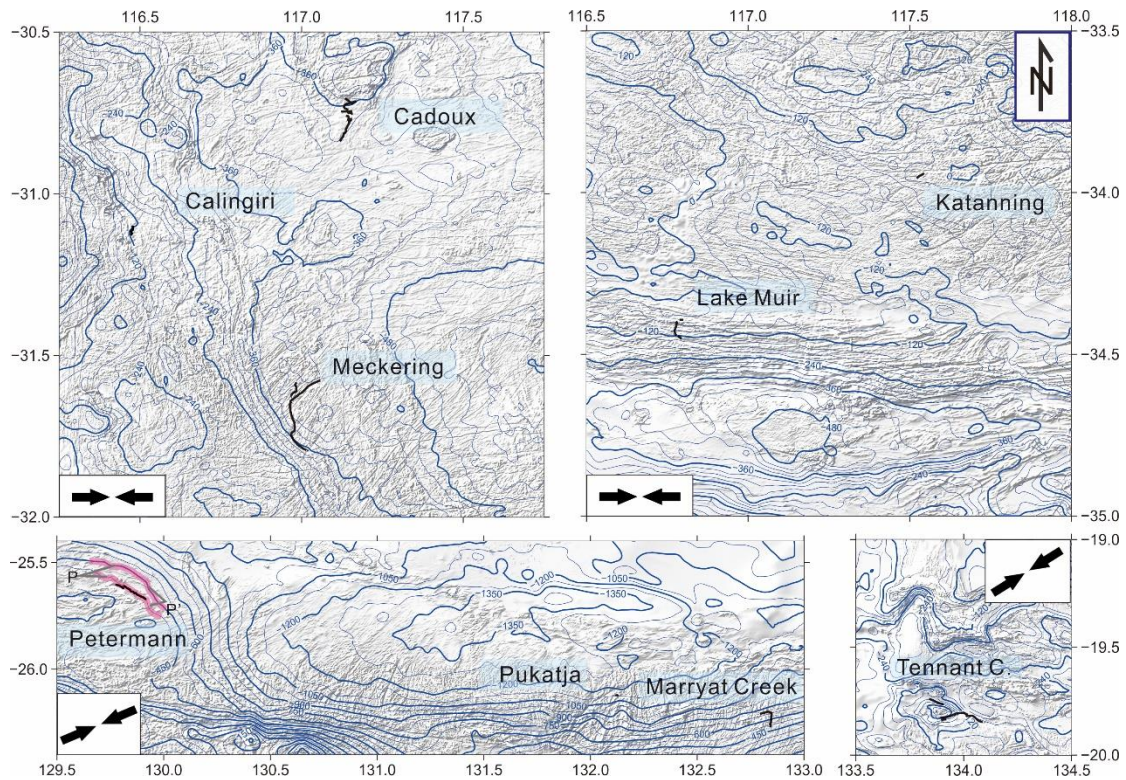


1447

1448 **Figure 8.** (A) Total magnetic intensity map shows how lineaments affect the

1449 development of surface ruptures. The uninterpreted map is put adjacent to the

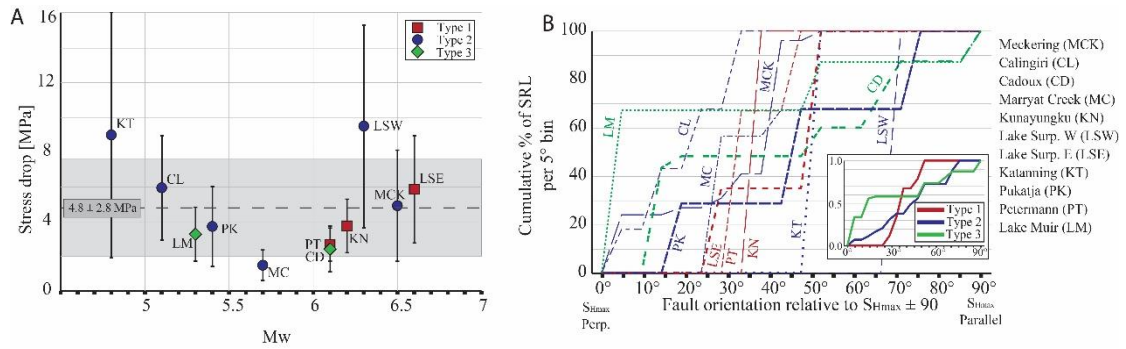
1450 interpreted map. Based on the regional  $S_{Hmax}$  orientation, the 11 events are divided into  
1451 two groups: (1) the Petermann, Pukatja, Marryat Creek and Tennant Creek events with  
1452 an average azimuth of  $21^\circ - 32^\circ$  and (2) the Cadoux, Meckering, Calingiri, Katanning  
1453 and Lake Muir events with an east-west oriented  $S_{Hmax}$ . The area in each sub-plot has  
1454 the same scale of  $0.6^\circ \times 0.6^\circ$ . The Spl. in Meckering is short for the secondary Splinter  
1455 rupture. (B) The sketch model illustrates how the orientation of  $S_{Hmax}$  orientation with  
1456 respect to lineaments (weak zones) may affect the surface rupture complexity.  
1457



1458

1459        **Figure 9.** (A) Bouguer gravity anomaly (Unit:  $\mu\text{m s}^{-2}$ ) contours overlying the  
 1460 shading map of magnetic lineaments. The surface ruptures are drawn with black lines  
 1461 and their names are labelled adjacent to the rupture. The black arrows show regionally  
 1462 averaged SHmax. The red thick lines overlying the gravity contour near the Petermann  
 1463 rupture mark the steps of the contours at the points P and P'.  
 1464

1465



1466

1467 **Figure 10.** Relationship between stress drop and fault orientation for *Type 1, 2 and*

1468 3. (A) Stress drop relative to  $M_w$  with each event categorized into *Type*. Uncertainties

1469 for each stress drop are calculated based on all stress drop estimates (Table S6). Dashed

1470 line and grey box indicate the average stress drop  $\pm 1\sigma$ . (B) The cumulative percent of

1471 rupture length relative to  $S_{Hmax}$  for each event, and per *Type* (where 0° is  $S_{Hmax}$

1472 perpendicular and 90° is  $S_{Hmax}$  parallel). The number of segments assigned to each

1473 rupture are taken from King et al. (2019) and detailed in Table S8 – 10 and Fig. S3.

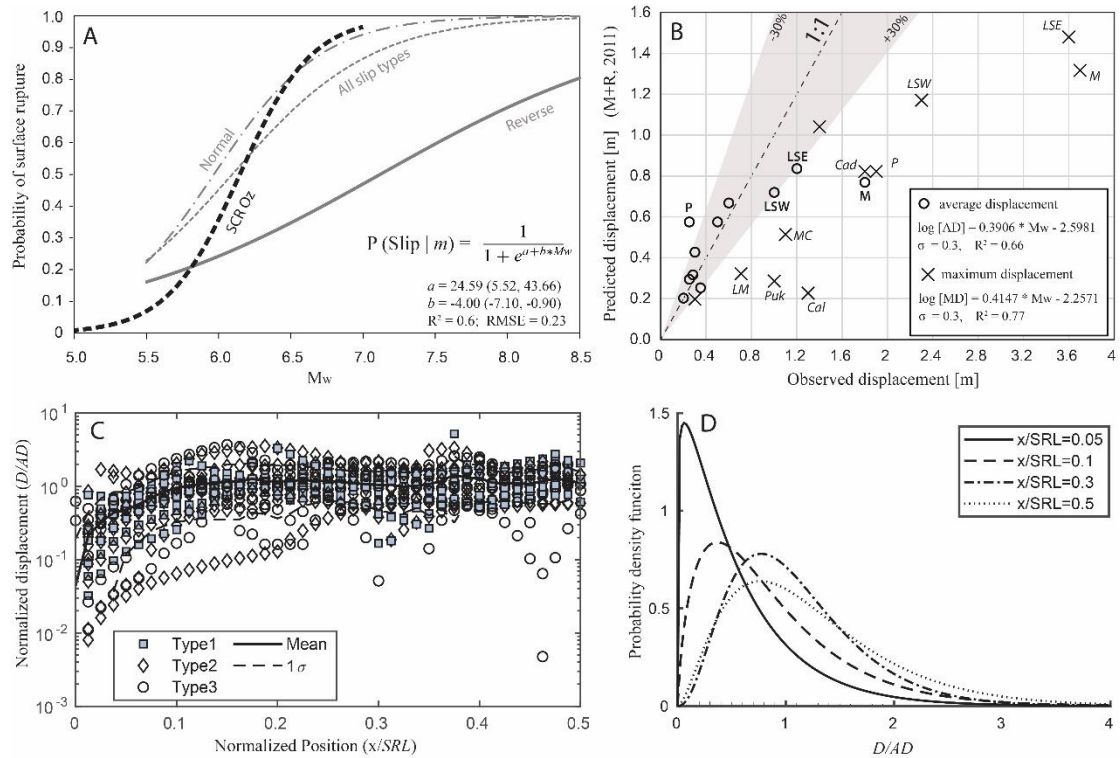
1474 While some *Type 2* and *3* events have well aligned segments (i.e. perpendicular to  $S_{Hmax}$ ),

1475 they generally have a larger range in orientations than *Type 1* events, which also have

1476 fewer segments.

1477

1478



1479

1480 **Figure 11.** A) Probability of surface rupture for reverse (from Moss and Ross,  
 1481 2011), normal (from Youngs et al., 2003), all slip kinematic types (from Youngs et al.,  
 1482 2003) and Australia SCR earthquakes (SCR Oz; this study). Empirical distributions are  
 1483 fit using logistic regressions; the SCR Oz curve is a best fit to a two-period moving  
 1484 average. The probability for all reverse faulting events is significantly lower than that  
 1485 of normal and all slip types for equivalent  $M_w$ , however the SCR Oz probability is  
 1486 significantly higher for equivalent  $M_w$ . Reverse, normal, and all distributions are only  
 1487 valid in the range of  $5.5 \leq M_w \leq 8.0$  and SCR Oz is valid only for  $4.0 \leq M_w \leq 6.6$ .

1488

1489 B) Predicted values for average ( $AD$ ) and maximum ( $MD$ ) surface rupture  
 1490 displacements from the equations of Moss and Ross (2011) plotted against the observed  
 1491  $AD$  and  $MD$  from King et al. (2019) and this study. The Moss and Ross (2011) equations

1492 are:  $LOG(AD) = 0.3244 * M_w - 2.2192$  and  $LOG(MD) = 0.5102 * M_w - 3.1971$ . The  
1493 1:1 line is flanked by  $\pm 30\%$  error bounds. Outlier datapoints are labeled in bold (*AD*)  
1494 and italics (*MD*): P = Petermann, LSE = Lake Surprise East, LSW = Lake Surprise West,  
1495 M= Meckering, LM= Lake Muir, Puk = Pukatja, Cal = Calingiri. New  $M_w$ -based  
1496 regression fits for *AD* and *MD* based only on the Australian SCR data appear in the  
1497 legend; given that 9 of 11 Australian earthquakes have observed *MD* >> modelled  
1498 (Ross and Moss, 2011) *MD*, these new regressions may preferred for SCR PFDHA  
1499 analyses.

1500

1501 C) Normalized displacement (discrete displacement / *AD*) for Australian SCR  
1502 earthquakes plotted as a function of rupture half length ( $x/L$ , where  $x/L = 0$  is the rupture  
1503 tip and  $x/L = 0.5$  is the rupture mid-point).

1504

1505 D) Gamma distributions for spatial variability in *AD* at different normalized  
1506 positions (most proximal to rupture tip,  $x = 0.05$ ; rupture mid-point,  $x = 0.5$ ). These  
1507 distributions may be used to obtain an *AD* probability distribution for PFDHA at  
1508 specific sites (e.g., Moss and Ross, 2011); intermediate positions along the fault will  
1509 have intermediate profiles.

1510